

1 **Improved representation of river runoff in Estimating the**
2 **Circulation and Climate of the Ocean Version 4 (ECCOv4)**
3 **simulations: implementation, evaluation, and impacts to**
4 **coastal plume regions**
5

6 Yang Feng^{1,2,3}, Dimitris Menemenlis⁵, Huijie Xue^{1,2}, Hong Zhang⁵, Dustin Carroll^{6,5},

7 Yan Du^{1,2,4}, Hui Wu⁷
8

9 1. State Key Laboratory of Tropical Oceanography, South China Sea Institute of Oceanology &
10 Institution of South China Sea Ecology and Environmental Engineering, Chinese Academy of
11 Science, Guangzhou, China

12 2. Southern Marine Science and Engineering Guangdong Laboratory, Guangzhou, China

13 3. Guangdong Key Laboratory of Ocean Remote Sensing, South China Sea Institute of Oceanology,
14 Chinese Academy of Sciences

15 4. College of Marine Science, University of Chinese Academy of Sciences, Guangzhou, China

16 5. Jet Propulsion Laboratory, California Institute of Technology, Pasadena, California, USA

17 6. Moss Landing Marine Laboratories, San José State University, Moss Landing, California, USA

18 7. State Key Laboratory of Estuarine and Coastal Research, East China Normal University, Shanghai,
19 China

20 *Correspondence to:* Yang Feng (yfeng@scsio.ac.cn)
21
22

23 **Abstract**

24 In this study, we improve the representation of global river runoff in the Estimating the Circulation and
25 Climate of the Ocean Version 4 (ECCOV4) framework, allowing for a more realistic treatment of
26 coastal plume dynamics. We use a suite of experiments to explore the sensitivity of coastal plume
27 regions to runoff forcing, model grid resolution, and grid type. The results show that simulated Sea
28 Surface Salinity (SSS) is reduced as the model grid resolution increases. Compared to Soil Moisture
29 Active Passive (SMAP) observations, simulated SSS is closest to SMAP when using Daily, Point-
30 source Runoff (DPR) and the intermediate-resolution LLC270 grid. The Wilmott skill score, which
31 quantifies agreement between models and SMAP, yields up to 0.92 for large rivers such as the Amazon
32 River. There was no significant difference in SSS for tropical and temperate coastal rivers when the
33 model grid type was changed from ECCO v4 latitude-longitude-polar cap grid to ECCO2 cube-sphere
34 grid. We also found that using DPR forcing and increasing model resolution from the coarse-resolution
35 LLC90 grid to the intermediate-resolution LLC270 grid elevated the river plume area and volume,
36 stabilized upper-layer stratification, and shoaled the mixed layer depth (MLD). Additionally, we find
37 that the impacts of increasing model resolution from intermediate-resolution LLC270 grid to high-
38 resolution LLC540 grid are regionally dependent. The Mississippi River Plume is more sensitive than
39 other regions, possibly because the broader and shallower Texas-Louisiana shelf drives a more
40 substantial baroclinic effect, and relatively weak sub-grid scale vertical mixing and adjustment in this
41 region. Since rivers deliver enormous amounts of freshwater and anthropogenic materials to coastal
42 areas, we believed that improving the representation of river runoff in global, high-resolution ocean
43 models will advance studies of coastal hypoxia, carbon cycling, and regional weather and climate, and
44 ultimately help to predict land-ocean-atmospheric feedbacks seamlessly in the next generation of earth
45 system models.

46

47

48

49

50 **1 Introduction**

51 Coastal plume regions represent a small fraction of Earth's surface but play an active role in the
52 global cycling of carbon and nutrients (Bourgeois et al., 2016; Carroll et al., 2020; Fennel et al., 2019;
53 Lacroix et al., 2020; Landschützer et al., 2020; Roobaert et al., 2019). Recent satellite-based observations
54 with quasi-global coverage have been greatly improved to monitor Sea Surface Salinity (SSS), a key
55 tracer for tracking the river plumes. The European Space Agency (ESA) Soil Measure and Ocean Salinity
56 (SMOS; Mecklenburg et al., 2012) with 33-km/10-day and National Aeronautics and Space
57 Administration (NASA) Soil Moisture Active Passive (SMAP) missions with 40-km/8-day space/time
58 gridding acquire SSS observations with sufficient resolution to track the plume pathways and to analyze
59 the underlying dynamics (Fournier et al. 2016a, b; 2017a,b; 2019; Gierach et al. 2013; Liao et al., 2020).
60 To date, however, coastal plume regions have not been explicitly resolved in most global Ocean General
61 Circulation Models (OGCMs), Earth System Models (ESMs), and Global Ocean Data Assimilation
62 System (GODAS) products (Ward et al., 2020). As a result, plume regions simulated by OGCMs, ESMs,
63 and GODAS are not consistent with satellite observations. For example, Fournier et al. (2016a) found
64 that the 1/12° global circulation Hybrid Coordinate Ocean Model (HYCOM) did not accurately capture
65 SSS during extreme flood events in the northern Gulf of Mexico. Denamiel et al. (2013) found that the
66 Congo River nearshore SSS in global HYCOM was underestimated compared to other regional
67 simulations, even though the models had comparable horizontal grid resolution. Santini and Caporaso
68 (2018) suggested that most CMIP5 models might lack skill in representing the Congo River Basin runoff
69 and SSS in the vicinity of river mouths. Most OGCMs, ESMs, and GODAS products usually have large
70 horizontal grid cells, and only a few cells may encompass the entire plume. As a result, freshwater
71 delivered to these cells is thoroughly mixed and diluted, and therefore cannot represent the complex
72 plume dynamics. Additionally, for the riverine freshwater input, the ocean is forced in the top model
73 layer over a pre-determined surface area in the vicinity of river mouths, usually specified with a
74 climatological signal. Thus, the system disturbances by extreme weather events, e.g., floods and droughts,
75 cannot be explicitly resolved (Griffies et al. 2005; Tseng et al. 2016). Finally, virtual salt fluxes have
76 been widely employed, where freshwater affects salinity without a change in mass or volume flux
77 (Bentsen, 2013; Halliwell, 2004; Timmermann et al., 2009; Volodin et al., 2010). The above model
78 configurations limit the representation of coastal plume region in global scale models.

79 Estimating the Circulation and Climate of the Ocean (ECCO) is a data assimilating model that uses
80 observational data to make the best possible estimates of ocean circulation and its role in climate. The
81 model uses the cube-sphere (ECCO2) and latitude-longitude-polar-cap (ECCOv4) grids for global
82 application. Like most OGCMs, ESMs, and GODAS products, the current ECCO simulations route
83 riverine freshwater from land directly to the ocean by using observed river runoff as a seasonal
84 climatological mass flux over the top of several surface grid cells near the river mouths (Fekete et al.
85 2002; Stammer et al.2004). Recent ECCO efforts have been extended to address the global-ocean
86 estimates of pCO₂ and air-sea carbon exchange (Carroll et al. 2020). The model resolution has been
87 promoted as fine as 1-km globally to investigate mesoscale-to-submesoscale dynamics in the open ocean
88 (Su et al., 2018). However, the current ECCO lacks representation of coastal interfaces and related
89 feedbacks, which limits their application to global climate change and further impeding our ability to
90 make informed resource management decisions. In this study, we here improved the representation of
91 river runoff in ECCO and systematically evaluate model performance in reproducing SSS within the
92 vicinity of large tropical and temperate river mouths. We also investigated the impact of runoff forcing,
93 model grid resolution, and grid type on coastal dynamics and key plume physical properties. This work
94 aims provide a comprehensive sensitivity analysis of runoff forcing in multiple simulations, which will
95 help develop global ECCO simulations that more robustly represent the Land-Ocean-Aquatic-Continuum
96 (LOAC).

97 The paper is organized as follows. Section 2 briefly introduces ECCO and the various runoff forcing
98 methods used in this study. Section 3 provides a comprehensive evaluation of model sensitivity to
99 horizontal grid resolution and river forcing. Section 4 discusses the sensitivity of plume properties and
100 coastal stratification. Results are summarized in Section 5.

101 **2 Methods**

102 **2.1 ECCO Simulations and Representation of River Runoff**

103 In this study, we employ the Massachusetts Institute of Technology general circulation model
104 (MITgcm; Marshall et al., 1997) in several model configurations developed for the ECCO project
105 (Menemenlis et al., 2005; Forget et al., 2015; Zhang et al., 2018). The ECCO MITgcm configurations
106 that we use herein solve the hydrostatic, Boussinesq equations on either Cubed Sphere (CS; Adcroft et
107 al., 2004) or Latitude-Longitude-polar-Cap (LLC; Forget et al., 2015) grids. The cubed-sphere
108 configuration is the so-called CS510 grid, which was developed for the ECCO2 project (Menemenlis et

109 al., 2008), consisting of 6 faces with 510×510 dimensions. It has a quasi-homogeneous horizontal grid
110 spacing of 20 km. We also consider three different LLC grid configurations: LLC90, LLC270, and
111 LLC540, which have 1° , $1/3^\circ$, and $1/6^\circ$ nominal horizontal grid spacing, respectively. The LLC grids are
112 aligned with lines of latitude and longitude between 70° S and 57° N with grid spacing varying with
113 latitude. We use LLC# horizontal grids for our experiments, where the # is the number of points along
114 one-quarter of the equator. Therefore, LLC90 means 360 grid points circle the equator. The model has
115 50 vertical z-levels; the vertical resolution is 10 m in the top 7 levels and telescopes to 450 m at depth.
116 This setup was the same for all designed experiments. We use a third-order, direct-space-time (DST-3)
117 advection scheme, while vertical advection uses an implicit third-order upwind scheme. Vertical mixing
118 is parameterized using the Gaspar-Grégoris-Lefevre (GGL) mixing-layer turbulence closure and
119 convective adjustment scheme (Gaspar et al., 1990). Lateral eddy viscosity in ECCOv4 is harmonic, with
120 a coefficient of $0.005L^2/\Delta t$, where L is the grid spacing in meters and $\Delta t = 3600s$. Depending on
121 location, the resulting eddy viscosity varies from $\sim 10^3$ to $\sim 1.6 \times 10^4 m^2s^{-1}$. Additional sources of
122 dissipation in ECCOv4 are from harmonic vertical viscosity and quadratic bottom drag, and contributions
123 from the vertical mixing parameterization. A detailed description of ECCOv4 is provided in Forget et al.
124 (2015).

125 ECCOv4 uses natural boundary conditions for both the river discharge and E-P (evaporation minus
126 precipitation) (Huang 1993; Roulet and Madec; 2000). The runoff is applied as a real freshwater flux
127 forcing, which allows for material exchanges through the free surface and more precise tracer
128 conservation compared to virtual salt flux boundary conditions (Campin et al., 2008). The model uses
129 z^* rescaled height vertical coordinates (Adcroft and Campin, 2004) and the vector-invariant form of the
130 momentum equation (Adcroft et al., 2004). With z^* coordinates, variability in free surface height is
131 distributed vertically over all grid cells. For a water column that extends from the bottom at $z = -H$ to
132 the free surface at $z = \eta$, the z^* vertical coordinate is defined as $z = \eta + s^*z^*$, where $s^* = 1 + \eta/H$
133 is the rescaling factor. The Boussinesq, depth-dependent equations for conservation of volume and
134 salinity under the vector-invariant form of the momentum equations are:

$$135 \quad \frac{1}{H} \frac{\partial \eta}{\partial t} + \nabla_{z^*} \cdot (s^* v) + \frac{\partial w}{\partial z^*} = s^* F \quad (1)$$

$$136 \quad \frac{\partial (s^* S)}{\partial t} + \nabla_{z^*} \cdot (s^* S v_{res}) + \frac{\partial (S w_{res})}{\partial z^*} = s^* (D_{\sigma, S} + D_{v, S}) \quad (2)$$

137 where F is the surface freshwater flux (includes both precipitation minus evaporation and river runoff),
 138 ∇_{z^*} is the gradient operator on z^* plane. S is the potential salinity, $D_{v,S}$ and $D_{\sigma,S}$ are subgrid-scale
 139 processes parameterized as mixing diapycnal and along the isoneutral surface, which respect the highly
 140 adiabatic process of the oceanic interior (Griffies et al. 1998). The v_{res} and w_{res} are the horizontal and
 141 vertical residual mean velocity fields and hold the relationship $(v_{res}, w_{res}) = (v, w) + (v_b, w_b)$, where
 142 (v_b, w_b) is the bolus velocity parameterizing the effect of unresolved eddies (Gent and McWilliams,
 143 1990). Our daily, point-source runoff (DPR) experiments add freshwater to a single model grid cell in
 144 the first vertical model layer, while the diffuse climatological runoff experiments add it over multiple
 145 horizontal grid cells in the top layer. The amount of freshwater added to each model grid cell decreases
 146 exponentially as a function of distance from river outlets.

147 **2.2 Sensitivity Experiments**

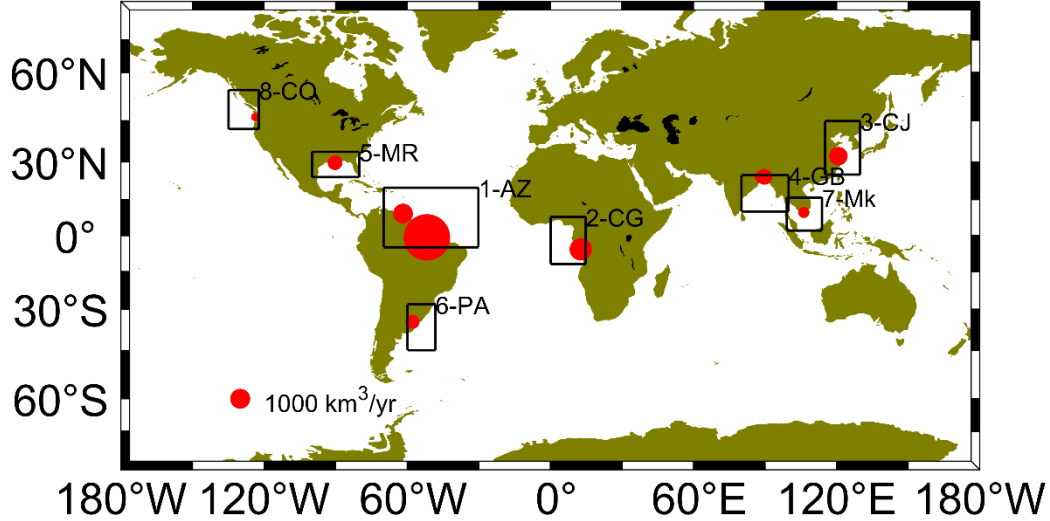
148 We first run seven experiments, derived from the ECCOv4 set-up, to test the sensitivity of SSS in
 149 the vicinity of large river mouths to ECCOv4 model grid resolution and runoff forcing (Table 1). The
 150 initial condition of ECCOv4 was from optimized adjustment of Mapping Ocean Observations in a
 151 Dynamical Framework: A 2004-06 Ocean Atlas (OCAA) and surface forcing was from adjustment of
 152 ECMWF Re-Analysis (ERA) interim. The LLC90, LLC270, and LLC540 corresponds to coarse ($1^\circ /$
 153 ~ 100 km), intermediate ($1/3^\circ / \sim 40$ km), and high ($1/6^\circ / \sim 20$ km) resolution from low- to mid-
 154 latitudes, respectively. LLC90C and LLC270C are forced by monthly climatological runoff from Fekete
 155 et al. (2002). The runoff has a spatial resolution of $\sim 1^\circ$ and was linearly interpolated to each grid cell.
 156 Therefore, runoff may be fluxed into a single grid cell in the coarse-resolution run and over several grid
 157 cells in the high-resolution run. The twin experiments, LLC90R and LLC270R, the highest resolution
 158 run LLC540R, use Japanese 55-year atmospheric reanalysis (JRA55-DO) river forcing dataset (Suzuki
 159 et al., 2017; Tsujino et al., 2018). JRA55-DO includes daily river runoff is generated by running a global
 160 hydrodynamic model forced by adjusted land-surface runoff. Comparing to the Fekete ECCOv4 runoff,
 161 JRA55-DO runoff has daily output; therefore, it can resolve interannual variability and extreme floods
 162 and drought events. We add JRA55-DO runoff as point source flux at a single grid cell adjacent to river
 163 outlets for LLC90/270/540R. For the intermediate-resolution LLC270 run, we did two additional
 164 experiments: LLC270R_spread and LLC270R_clim. The LLC270R_spread used daily JRA55DO river
 165 discharge, but forced over several grid cells, which allows the model to automatically interpolate the
 166 runoff. The LLC270C_clim used single grid cell point-source surface forcing, but with climatological

167 runoff derived from 2015–2017. The additional experiments were conducted because the widely-used
 168 climatological runoff by Fekete et al. (2002) in ECCOv4 differed from JRA55DO climatology. A
 169 comparison between LLC90C vs LLC270C, or LLC90R vs LLC270R vs LLC540R shows the resolution
 170 impacts. A comparison between LLC270R_spread and LLC270R shows the pure difference of adding
 171 runoff to a single grid cell (point-source runoff) vs multiple grid cell (diffusive runoff). In addition to the
 172 LLC grid, two additional experiments are conducted on the widely-used cube-sphere ECCO2 grid to
 173 investigate model sensitivity to the choice of grid topology (Table 1). CS510C is an ECCO2 run with
 174 monthly climatological runoff from Stammer (2004). The Stammer runoff is spread over a pre-
 175 determined surface area in the vicinity of river mouths. The spreading radius decreases exponentially
 176 with a 1000-km e-folding distance. Spatial fields of runoff forcing for ECCOv4, ECCO2, and JRA55-
 177 DO are shown in Figure S1.

#	Experiment Name	Grid Type	Runoff Forcing	Grid spacing
1	LLC90C	Lat-Lon-Cap	ECCOv4 Climatology	55–110 km
2	LLC90R	Lat-Lon-Cap	JRA55-do	55–110 km
3	LLC270C	Lat-Lon-Cap	ECCOv4 Climatology	18–36 km
4	LLC270R	Lat-Lon-Cap	JRA55-do	18–36 km
5	LLC270R_spread	Lat-Lon-Cap	JRA55-do	18–36 km
6	LLC270R_clim	Lat-Lon-Cap	JRA55-do	18–36 km
7	LLC540R	Lat-Lon-Cap	JRA55-do	9–18 km
8	CS510C (Standard ECCO2)	Cube-sphere	ECCO2 Climatology	~19 km
9	CS510R	Cube-sphere	JRA55-do	~19 km

178
 179 **Table 1:** Summary of all experiments. The ECCOv4 and ECCO2 climatological runoff is derived from
 180 Fekete et al. 2002 and Stammer et al. 2004, respectively. A comparison of runoff forcing is shown in
 181 Figure S1.

182 Each sensitivity experiment is integrated for 26 years (1992–2017), and we analysed the final 3-
 183 year period (1 January 2015 to 31 December 2017). We begin our analysis in January 2015 because the
 184 high-resolution SMAP observations, which we use to evaluate model skill, are began on 1 April 2015.
 185 10 large rivers at 8 coastal regions spanning from low- to mid-latitudes are selected for detailed analysis;
 186 including the Amazon and Orinoco (AZ), Congo (CG), Changjiang (CJ), Ganges and Brahmaputra (GB),
 187 Mississippi (MR), Parana (PA), Mekong (MK), and Columbia (CO) rivers (**Figure 1**).



188

189 **Figure 1:** The 10 large rivers (red circles) at 8 coastal regions (black boxes) used in our analysis: Amazon
 190 and Orinoco (South America, noted as region 1), Congo (Africa, region 2), Changjiang (Asia, region 3),
 191 Ganges and Brahmaputra (Asia, region 4), Mississippi (North America, region 5), Parana (South America,
 192 region 6), Mekong (Asia, region 7), Columbia (North America, region 8). Red circle size is scaled by the
 193 climatological river discharge magnitude.

194

195 **2.3 Target Diagram and Willmott Skill Score**

196 The first part of our study compares the simulated salinity with the synchronized SMAP SSS
 197 observations from 1 April 2015 to 31 December 2017 at the river mouth region (Section 3). The level 3
 198 SMAP version-3 SSS was produced by the Jet Propulsion Laboratory (<ftp://podaac-ftp.jpl.nasa.gov> Yueh
 199 et al., 2013, 2014). We also compare climatological SSS during this period with the World Ocean Atlas
 200 2018 (<https://www.nodc.noaa.gov/OC5/woa18/>). We use the Willmott skill score (Willmott, 1981), a
 201 widely-used metric for quantifying agreement between models and observations. The Willmott score is
 202 calculated as:

203
$$W_{skill} = 1 - \frac{\sum_{i=1}^n (M_i - O_i)^2}{\sum_{i=1}^n (|M_i - \bar{O}| + |O_i - \bar{O}|)^2} \quad (3)$$

204 where M_i is the model estimate at t_i , O_i is the observation at time t_i , \bar{O} is the mean of the observations,
 205 and n is the number of time records for comparison. Specifically, $W_{skill} = 1$ indicates perfect agreement
 206 between model and observations; $W_{skill} = 0$ indicates that the model skill is equivalent to the
 207 observational mean.

208 Furthermore, we conduct our skill assessment for model SSS on multiple experiments across several
 209 regions. We also use Target diagrams (Jolliff et al. 2009) to visualize a suite of skill metrics efficiently.
 210 Target diagrams are plotted in a Cartesian coordinate system with the x-axis representing the unbiased

211 root-mean-square-deviation (RMSD), the y-axis represents the bias, and the distance between the origin
 212 and any point within the Cartesian space representing total RMSD.

$$213 \quad Bias = \frac{\sum_{i=1}^n (M_i - O_i)}{n} = \bar{M} - \bar{O} \quad (4)$$

$$214 \quad Unbiased \ RMSD = \sqrt{\frac{\sum_{i=1}^n [(M_i - \bar{M}) - (O_i - \bar{O})]^2}{n}} \quad (5)$$

$$215 \quad RMSD = \sqrt{\frac{\sum_{i=1}^n (M_i - O_i)^2}{n}} \quad (6)$$

216 \bar{M} represents the mean of the model estimates. These three skill assessment statistics are
 217 particularly useful, as bias reports of the size of the model-observation discrepancies. Bias values near
 218 zero indicate a close match, though it can be misleading as negative and positive differences can cancel
 219 each other. The unbiased RMSD removes the mean and is a pure measure of how model variability differs
 220 from observational variability. The total RMSD provides an overall skill metric, as it includes
 221 components for assessing both the mean (bias) and the variability (unbiased RMSD).

222 We normalize the bias, unbiased RMSD, and total RMSD by the observational standard deviation
 223 (σ_o) to allow for the display of multiple experiment and regional SSS observations on a single Target
 224 Diagram. According to the definition of unbiased RMSD, the value should always be positive. However,
 225 the $X < 0$ region of the Cartesian coordinate space may be utilized if the unbiased RMSD is multiplied
 226 by the sign of the standard deviation difference (σ_d):

$$227 \quad \sigma_d = sign(\sigma_m - \sigma_o) \quad (7)$$

228 The resulting target diagram thus provides information about whether the model standard deviation is
 229 larger ($X > 0$) or smaller ($X < 0$) than the observations' standard deviation, in addition to if the model
 230 mean is larger ($Y > 0$) or smaller ($Y < 0$) than the observations' mean.

231 **2.4 Definition of plume characteristics**

232 We investigate the role of grid resolution and runoff forcing through several key metrics: plume
 233 area, volume, and freshwater thickness. The plume area is defined as regions with SSS below a given
 234 salinity threshold S_A (See Sect. 4.2). The freshwater volume, relative to the reference salinity, S_0 , is
 235 defined as the integral of the freshwater fraction

$$236 \quad V_f(S_A) = \iiint_{s < S_A} \frac{s_0 - s}{s_0} dV \quad (8)$$

237 where the volume integral is bounded by the isohaline S_A . Here, we assume the maximum salinity in
238 each selected region as the reference salinity S_0 . The freshwater thickness δ_{fw} represents the equivalent
239 depth of freshwater and is computed as:

$$240 \quad \delta_{fw} = \int_{-h}^{\eta} \frac{S_0 - S}{S_0} dz \quad (9)$$

241 $S(z)$ is the depth-dependent diluted salinity due to the river discharge, η is the sea level, and h is the
242 bottom depth.

243 **3. Comparison with SMAP and WOA18**

244 We first estimate how various ECCOv4 LLC simulations (Table 1) compare to observations in the
245 vicinity of 10 large river mouths. The synchronized SMAP SSS (01 April 2015 to 31 December 2017,
246 33-month) is used as the primary verification dataset (Yueh et al., 2013, 2014). SMAP SSS has been
247 documented to exhibit bias compared to observed SSS in shallow waters near river mouths (Fournier et
248 al., 2017). Therefore, as an indication of real SSS, we also compare the model simulations to the World
249 Ocean Atlas 2018 (WOA18), which is an objective analysis of in-situ observations from a period of
250 “climate normal” years (1981-2010) (Zweng et al., 2019). We note that there may be relatively few
251 observations incorporated into the objectively-analysed WOA18 product near the coast, which may over-
252 smooth salinity fronts. Additionally, WOA18 is a 55-year climatology from 1955–2010; therefore, we
253 can only compare model climatology from 2015–2017. Overall, we use SMAP and WOA18 as
254 “observational references”, where our model-observation comparisons provide useful information on
255 how SSS changes between experiments rather than determine which experiment is closer to the real
256 world.

257 The upper 10-m SSS biases relative to SMAP, averaged over the 33 months, for CS510C (standard
258 ECCO2) and the LLC540R (highest resolution) are shown in Figure S2. Both SMAP and WOA18 have
259 $1/4^\circ$ horizontal grid resolution, therefore, we interpolated all model fields to this grid. For both
260 simulations, negative biases are found from low- to mid-latitudes, while positive biases occur at high
261 latitudes. When focusing on large river mouth regions (e.g., AZ, PA, and CJ), the SSS bias is reduced in
262 LLC540R. This demonstrates that the choice of runoff forcing impacts on SSS at predominantly local
263 scales; however, background currents can transport the signal downstream or offshore to the open ocean
264 (Liu et al., 2009; Molleri et al., 2010).

265 Next, we compute the mean model SSS near all selected river mouth regions, along with SMAP
266 and WOA18 (Table 2). The corresponding Willmott Skill (WS) numbers are listed in Table 3. We use

267 the 1st Empirical Orthogonal Function (EOF) derived from WOA18 to determine river mouth regions,
268 since WOA18 represents persistent low-salinity zones over the 30 years. We remove the mean SSS field
269 before the EOF analysis. The 1st mode explains ~47–67% of the total variance. We then reconstruct the
270 dominant SSS anomaly field by multiplying the 1st PC with the spatial pattern. Locations with salinity
271 that is 1–2 PSU lower in the reconstructed SSS field is taken as the river mouth region, and all eight
272 regions are shown in Figure S3. The SMAP SSS has been found lower than the WOA18 SSS for large
273 rivers. The underestimation is more than 5 PSU for the Amazon region. The deviation between satellite
274 products and in-situ observations is consistent with Fournier et al. (2016) and Fournier et al. (2017).
275 Near the selected large river mouths, experiments with daily, point-source runoff forcing have lower SSS
276 than experiments forced by climatological diffusive runoff (LLC90R vs. LLC90C; LLC270R vs.
277 LLC270C; CS510R vs CS510C). Increasing model resolution generally results in regions becoming
278 fresher (Table 2; LLC90C to LLC270C; LLC90R to LLC270R to LLC540R). With the diffusive surface
279 forcing, LLC270R_spread driven by daily JRA55DO has lower salinity than LLC270C driven by Fekete.
280 This is not a surprise, since the model automatically interpolates the river forcing file to the model grids.
281 The Fekete river discharge file spreads spatially more than JRA55DO before the model interpolation
282 (Figure S1). This means less freshwater has been input to the top layer of the target river mouth region,
283 resulting in a relatively high salinity. Moreover, with the daily JRA55DO forcing, the sea surface salinity
284 with the point-source forcing (LLC270R) is lower than the diffusive forcing (LLC270R_spread). We can
285 think about adding river to single grid cell instead of multiple cells was equivalent to decreasing the inlet
286 width in regional models, which results in an increase in the inflow velocity, thus more efficiently
287 spreading riverine freshwater within our selected river mouth area (Table 2). Lastly, our new runs show
288 that with point-source river forcing, the runoff using year-by-year JRA55DO and climatological
289 JRA55DO produced inconsistent SSS changes for selected rivers. Specifically, in the experiments with
290 climatological JRA55DO, CG, CJ and PA river plumes have higher SSS, while AZ, GB, MR, MK and
291 CO river plumes have lower SSS.

292

River Mouth	Abb.	Discharge (m ³ /yr)	WOA	SMAP	LLC 90C	LLC 90R	LLC 270C	LLC 270R	LLC 270R_spread	LLC 270R	LLC 270R_clim	LLC 540R	CS 510C	CS 510R
Amazon/Orinoco	AZ	6440	32.7	27.5	34.0	34.1	31.7	30.4		28.2	27.6	24.6	34.3	23.8
Congo	CG	1270	33.6	33.7	34.7	34.3	34.6	35.3		33.9	35.2	33.7	34.9	34.1
Changjiang	CJ	907	32.9	31.4	33.1	32.8	33.0	33.2		32.2	32.4	31.8	32.5	30.9
Ganges/Brahmaputra	GB	643	29.3	27.5	30.9	29.4	29.5	27.6		27.2	27.1	23.9	29.7	25.6
Mississippi	MR	552	33.5	34.8	35.8	34.7	35.8	34.4		34.1	33.3	33.8	35.3	34.1
Parana	PA	517	28.9	27.3	33.7	31.0	31.1	24.9		24.7	25.5	20.0	33.8	20.0
Mekong	MK	504	32.9	32.9	33.5	32.6	32.3	31.2		30.3	29.8	31.0	31.8	28.5
Columbia	CO	167	30.7	31.0	32.0	31.7	31.7	31.3		30.8	30.5	30.3	31.4	30.4

294 **Table 2:** The SSS near river mouth for WOA18, SMAP, and all experiments for the selected regions

295

296 A comparison with SMAP shows that W_{skill} scores become higher when model resolution
 297 increases from 1° to $1/3^\circ$ (LLC90C vs LLC270C, LLC90R vs LLC270R), but lower when further
 298 increases to $1/6^\circ$ (e.g., LLC270R vs LLC540R for Amazon, Ganges/Brahmaputra, Parana). The higher
 299 or lower W_{skill} score is consistent with the SSS decrease. In the AZ region, SSS from LLC270R is ≤ 1
 300 PSU lower than the SMAP average, while LLC540R is ~ 3 PSU lower. Therefore, LLC270R receives a
 301 skill score of 0.92, higher than LLC540R (0.74). Although the SSS reduction lowers the model score
 302 overall, we should note that SMAP only has $1/4^\circ$ resolution. This means it may not have the capability
 303 to resolve the fine-scale dynamic features of the plume compared to high-resolution model simulations.
 304 In addition, SMAP may underestimate SSS near the river mouth (Fournier et al. 2017). Therefore, a
 305 larger discrepancy with SMAP in high resolution run does not indicate the simulation deviates from the
 306 truth.

307 When taking SMAP as the reference, the W_{skill} scores show that LLC270R_spread is better than
 308 LLC270C for most rivers, such as AZ, GB, MR, PA, and CO. This is not surprising since the JRA55DO
 309 runoff has better temporal resolution compared to Fekete runoff. As a comparison, W_{skill} scores of
 310 LLC270R_spread is worse than LLC270R. This is because diffusive surface runoff results in higher SSS
 311 than point-source surface runoff (Figure S8).

312 When taking WOA as the reference, experiments forced with the climatological river forcing
 313 (LLC270R_clim and LLC270C) had better W_{skill} score than daily forcing runs (LLC270R_spread and
 314 LLC270R). This is can be expected since WOA is a climatological dataset. A comparison with SMAP
 315 score shows that most ECCO SSS products had comparable skills with SMAP, indicating that they are
 316 reliable to use as a climatological mean.

317 The higher or lower W_{skill} score is consistent with how much the model deviates from the
 318 observational reference. At the AZ region, SSS from LLC270R is less than 1 PSU lower than the SMAP
 319 average, while LLC540R is roughly 3 PSU lower. Therefore, LLC270R receives a skill score of 0.92,
 320 higher than LLC540R (0.74). This also occurs with LLC270C and LLC270R when using WOA18 as the
 321 reference.

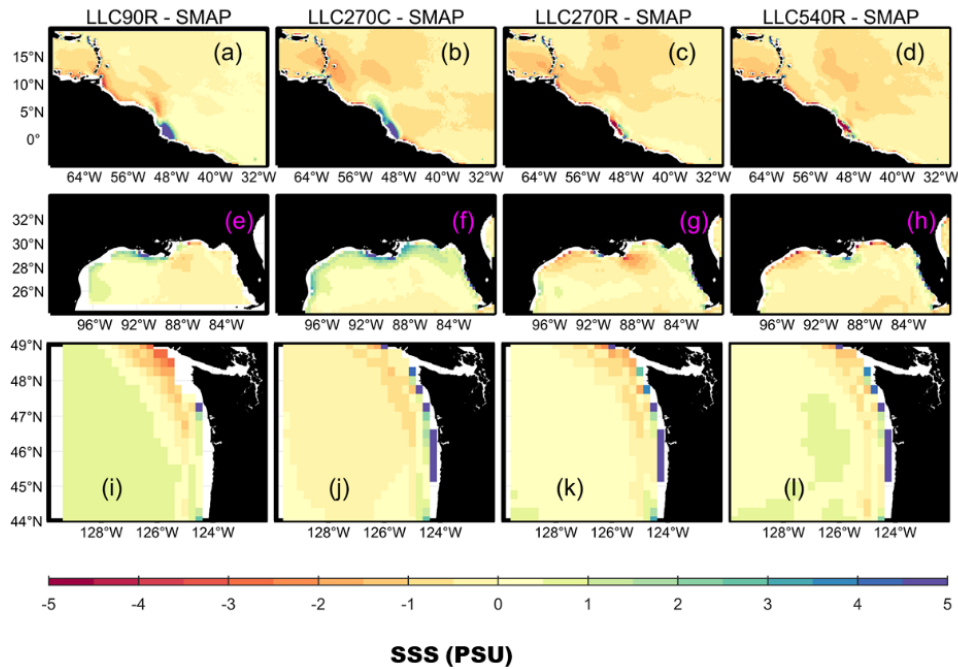
322 For rivers in tropical and temperate zones, the CS510 grid has a resolution comparable with the
 323 LLC540 grid. Therefore, the SSS and skill scores are comparable between CS510R and LLC540R. Since
 324 the model grid type has a negligible impact on SSS for low- to mid-latitude rivers, we will discuss model
 325 sensitivity to runoff forcing and model grid resolutions only.

River Mouth	SMAP	LLC 90C	LLC 90R	LLC 270C	LLC270R_ spread	LLC 270R	LLC270R_ clim	LLC 540R	CS 510C	CS 510R
with SMAP										
Amazon / Orinoco	-	0.50	0.50	0.71	0.83	0.92	0.92	0.79	0.46	0.73
Congo	-	0.58	0.64	0.69	0.46	0.89	0.47	0.88	0.60	0.87
Changjiang	-	0.53	0.59	0.51	0.50	0.64	0.31	0.83	0.59	0.85
Ganges / Brahmaputra		0.61	0.71	0.69	0.83	0.85	0.84	0.69	0.57	0.70
Mississippi		0.55	0.79	0.53	0.75	0.77	0.69	0.75	0.49	0.72
Parana		0.37	0.51	0.45	0.60	0.62	0.56	0.40	0.37	0.40
Mekong		0.79	0.90	0.77	0.67	0.54	0.47	0.63	0.74	0.38
Columbia		0.46	0.60	0.49	0.68	0.73	0.70	0.74	0.27	0.61
with WOA										
Amazon / Orinoco	0.47	0.73	0.69	0.87	0.62	0.64	0.78	0.47	0.54	0.44
Congo	0.54	0.60	0.67	0.70	0.48	0.94	0.47	0.95	0.64	0.92
Changjiang	0.44	0.82	0.94	0.68	0.70	0.70	0.73	0.72	0.78	0.54
Ganges / Brahamptura	0.73	0.72	0.90	0.92	0.77	0.78	0.82	0.51	0.73	0.59
Mississippi	0.69	0.46	0.59	0.46	0.76	0.68	0.60	0.73	0.49	0.66
Parana	0.87	0.40	0.45	0.45	0.42	0.42	0.42	0.29	0.40	0.29
Mekong	0.64	0.84	0.87	0.83	0.39	0.45	0.59	0.54	0.71	0.30
Columbia	0.47	0.51	0.62	0.63	0.85	0.87	0.82	0.84	0.51	0.90

326
 327 **Table 3:** The Willmott skill score for each run as compared with WOA18 and SMAP. The river mouth
 328 was recognized by the 1st EOF of WOA18 (See Figures 5 and S1). Note that WOA18 data are a 30- year
 329 climatology (1981—2010) and not in the same period as SMAP and experiments.
 330

331 To better compare the sensitivity of SSS to river forcing, we provide zoomed-in plots of the same
 332 comparison shown in Figure 1 for AZ, MR, and CO Rivers for all LLC simulations, representing large,

333 medium, and small rivers (Figure 2 and Figure S8). The positive bias is greatly reduced when applying
 334 daily, point-source river forcing, and increasing the horizontal grid resolution.



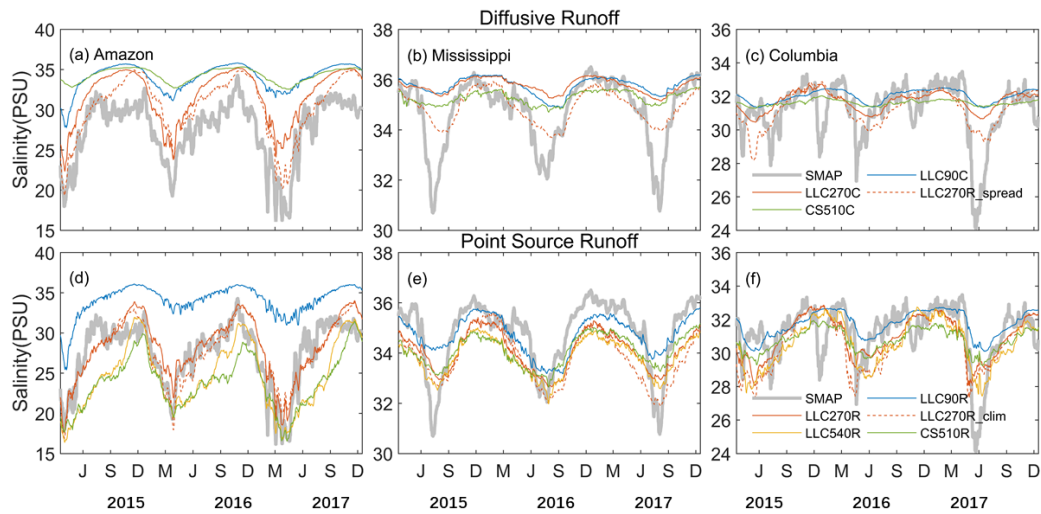
335

336 **Figure 2:** Zoomed-in view of SSS difference between model experiments and SMAP observations for
 337 large (Amazon, a–d), medium (Mississippi, e–h), and small (Columbia, i–l) rivers.
 338

339 Timeseries for all LLC simulations and SMAP at these three river mouths, are shown in **Figure 3**.

340 As in Figure 2, the bias decreases when daily, point-source river forcing is used and as the horizontal
 341 grid resolution increases. Additionally, the 2017 spring Amazon flood can be seen when forcing with
 342 diffusive daily JRA55DO (LLC270R_spread), but not by diffusive climatological Fekete case
 343 (LLC270C). The Mississippi/Columbia River mouth region is different from the Amazon in that the
 344 annual cycle of LLC270R_spread is stronger than LLC270C in all three years. This is because the
 345 seasonality of the Mississippi-Atchafalaya/Columbia River mouth has been oversmoothed in the
 346 climatological Fekete. The LLC270R_clim fluctuates in comparable with the LLC270R, except the
 347 annual extreme low SSS are comparable for the three simulated years.

348 Interestingly, the intermediate-resolution LLC270 run preforms better than the high CS510
 349 resolution run in the Amazon region. This is because the Stammer et al. (2004) runoff is spatially
 350 smoother and lacks seasonal variability compared to the Fekete et al. (2002) runoff in this region (Figure
 351 S7). When using DPR forcing, the SSS differences associated with the river discharge interannual
 352 variability can be resolved as well. For example, the 2017 abnormally-low SSS near the Amazon river
 353 mouth is associated with an extreme flooding event (Barichivich et al., 2018).



354

355 **Figure 3:** Area-averaged SSS in the Amazon, Mississippi, and Columbia river mouth regions (see Figure
 356 S3) with diffusive and point-source runoff forcing for SMAP (thick grey line) and experiments (thin
 357 coloured lines) with varying horizontal grid resolution. The method used to characterize the river mouth
 358 region is described in Section 3.

359

360 Next, we quantify the difference in mean and variance between the SSS time series of LLC

361 simulations and that of SMAP using daily JRA55DO runoff but with diffusive and point source method

362 for each (**Figure 4**). With the same daily JRA55DO, the normalized bias has been found lower in the

363 experiment with point sources than in the experiment with diffusive sources in general when forced with

364 daily JRA55DO. The change in normalized unbiased RMSD is largely negligible compared to the

365 changes in normalized bias for most rivers, except CG and MK. Most unbiased RMSD remains negative

366 when switching the runoff forcing from climatological to daily for most regions. This implies that the

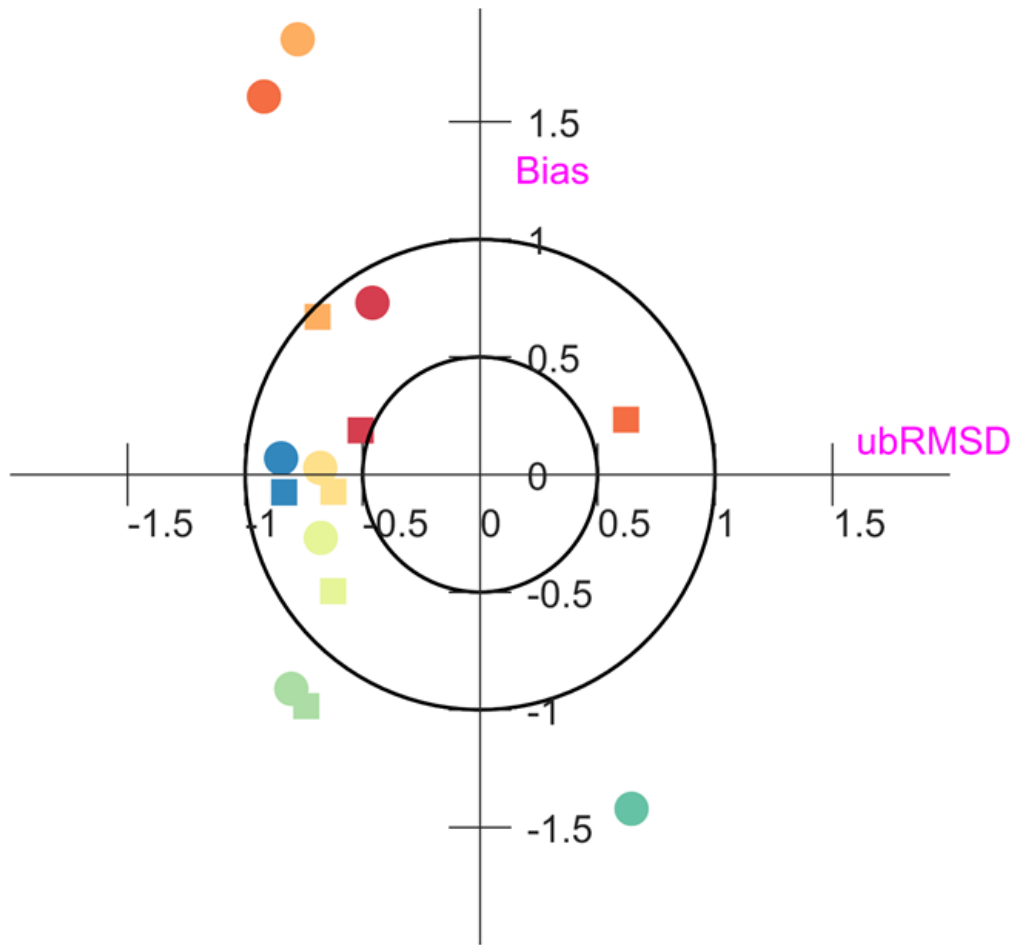
367 variance of LLC simulations remains lower than SMAP observations despite of the runoff forcing

368 changes. The exception of the CG River is possibility because it is a near equator eastern boundary plume

369 where freshwater transport distinguished from others (Palma and Matano, 2017), and the abnormal MK

370 may reflect SMAP data are contaminated by the land signal near Vietnam coast, introducing lots of noise

371 to the SSS timeseries.



● Amazon LLC270R_spread ● Mississippi LLC270R_spread ■ Amazon LLC270R ■ Mississippi LLC270R
● Congo LLC270R_spread ● Parana LLC270R_spread ■ Congo LLC270R ■ Parana LLC270R
● Changjiang LLC270R_spread ● Mekong LLC270R_spread ■ Changjiang LLC270R ■ Mekong LLC270R
● Brahmputura LLC270R_spread ● Columbia LLC270R_spread ■ Brahmputura LLC270R ■ Columbia LLC270R

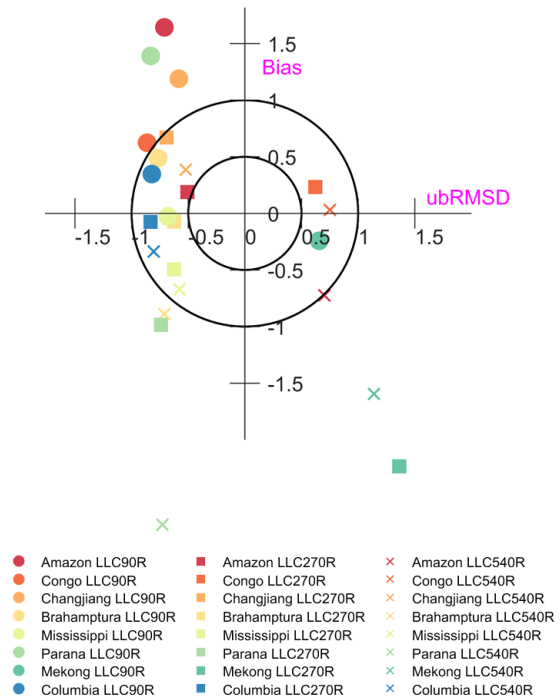
372
373
374
375
376

Figure 4: SSS target diagram near the selected river mouths (see Figure S3) for LLC270R_spread and LLC270R simulations.

377 We also examine the bias and variance on the Target Diagram for experiments with varying
 378 grid resolution but similar daily runoff forcing (**Figure 5**). Our results show that the normalized bias
 379 decreases as the model resolution increases, which is consistent with the SSS reduction in Table 2 and
 380 relatively low W_{skill} in Table 3. The unbiased RMSD decreases slightly, with the sign remaining
 381 negative as the model resolution increases. This occurs everywhere, except for the two largest rivers (AZ
 382 and CG) where the sign becomes positive for LLC540R, indicating that the model variance exceeds the
 383 SMAP variance when using the high-resolution grid. In summary, the comparison with synchronized

384 SMAP shows that using daily runoff and finer horizontal grid resolution improves the representation of
 385 SSS variability but at a cost of increased SSS bias.

386



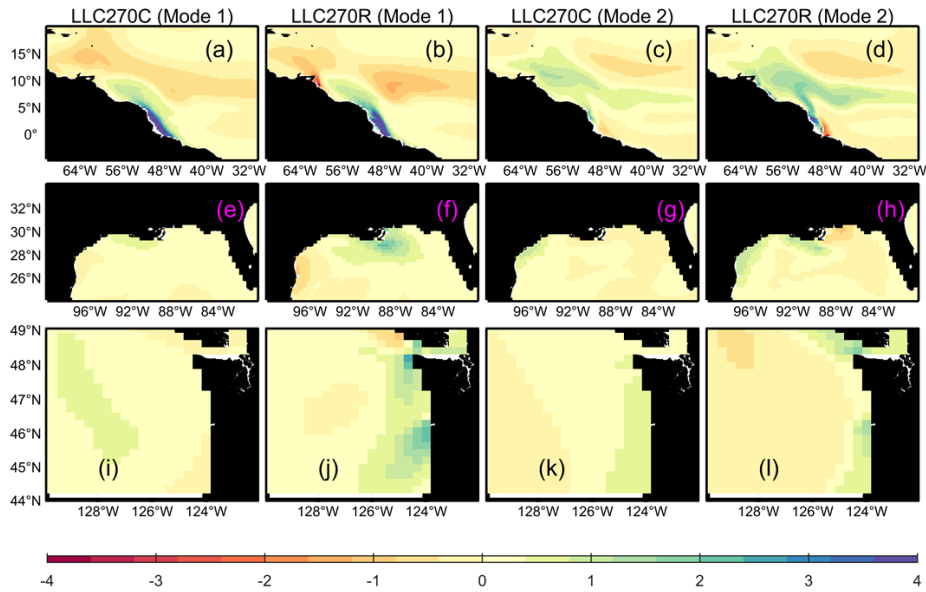
387

388 **Figure 5:** Same as Fig. 4, but for LLC90R, LLC270R, and LLC540R.

389 **4. Impact on River Plume Properties**

390 **4.1 EOF analysis of SSS**

391 We next investigate how model runoff improvements impact river plume properties such as plume
 392 area, volume, and freshwater thickness. Here, we focus on how the widely-used ECCOv4 simulation
 393 (forced by Fekete runoff) is different from the new DPR implementation. We limit our discussion to
 394 LLC#C/R cases only (Exp. 1, 2, 3, 4 and 7). We first evaluate plume SSS signature and dynamics through
 395 EOFs; the mean is removed before the EOF analysis. The first and second mode of AZ, MR, and CO
 396 using the same grid resolution but with different runoff forcing is shown in Figures 6 and S4. The spatial
 397 pattern reveals the salinity anomaly caused by the runoff, while the PC timeseries shows the timing. A
 398 single value in the spatial pattern or PC timeseries doesn't have an exact physical meaning, but together
 399 they reveal how much salinity deviates from the mean. The PC timeseries for experiments with DPR
 400 forcing clearly show similar seasonal cycles, albeit with larger amplitudes and interannual variability.



401

402 **Figure 6:** 1st and 2nd EOF spatial patterns from the LLC270C and LLC270R simulations for the Amazon,
 403 Mississippi, and Columbia rivers. The corresponding PC timeseries are normalized by the standard
 404 deviation and multiplied with the spatial mode.

405 For the AZ region, the LLC270R and LLC270C spatial patterns are similar for the first and second
 406 mode. The first mode accounts for 59% (72%) of the total variance in LLC270R (LLC270C). The spatial
 407 pattern reveals a low-salinity tongue; which located in a narrow band along the north-eastern South
 408 American coast from February–June, which is associated with the large river discharge and the
 409 northward-flowing North Brazil Current. The second mode of LLC270R (LLC270C) accounts for 33%
 410 (23%) of the total variance. The spatial pattern shows that the plume-like features extend northwestward
 411 to the Caribbean Sea and Central Equatorial Atlantic Ocean from May–September. This pattern is driven
 412 by Ekman currents associated with northeasterly wind stress and the transport to the Central Equator is
 413 due to the North Equatorial Counter Current (NECC, Lentz 1995a, b).

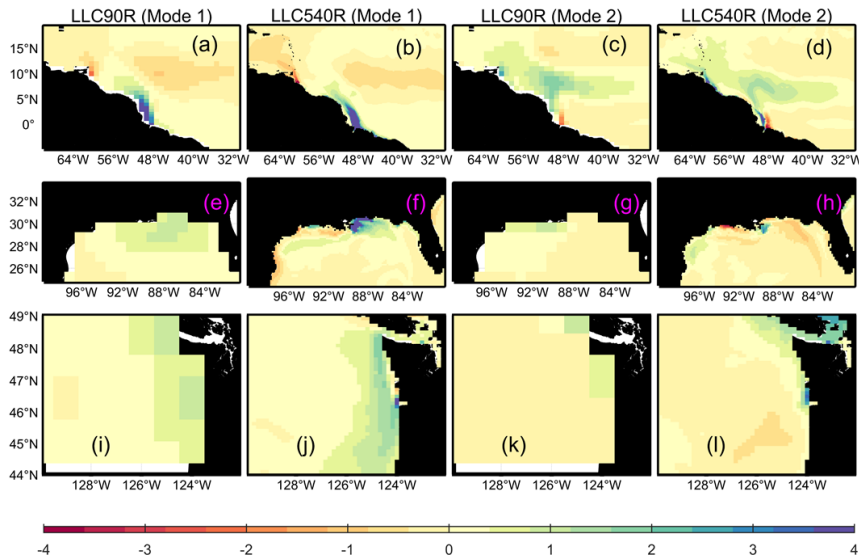
414 For the MR region, the first and second mode of LLC270R (LLC270C) explains 53% (66%) and
 415 29% (18%) of the total variance, respectively. The spatial pattern of the first mode is generally similar.
 416 There is a bulge-like plume feature that occupies a region near the MR mouth with a southeast extension
 417 to the central Gulf of Mexico from May–October (Figure S4), while the freshwater signal in the vicinity

418 of the southeast MR mouth is stronger in LLC270R. The extension of low-salinity waters is due to the
419 upwelling-favourable winds (southwesterly) from late-spring to summer, which transport the MR
420 freshwater offshore (Walker, 1996). The spatial pattern of the second EOF mode represents the low
421 salinity Mississippi River plume water transport downcoast from Louisiana towards Texas, which is
422 carried by the reversed shelf circulation from September to May (Cochrane and Kelly, 1986).

423 The first and second mode explains 63% (56%) and 29% (33%) of the variability at the CO region
424 in LLC270C (LLC270R), respectively. It has been previously recognized that the CO plume exhibits
425 seasonal variability forced by wind and freshwater discharge (García Berdeal *et al.*, 2002). During winter,
426 Ekman transport resulting from the northward winds constrains the plume against the Washington coast.
427 Downwelling-favorable wind stress strengthen the anti-cyclonic rotation of the river plume, resulting in
428 a coastally-attached winter plume. In contrast, prevailing southward wind stress results in offshore
429 Ekman transport; this advects the plume offshore, where it is influenced by the California Current over
430 long timescales and subsequently veers southward and offshore (Banas *et al.*, 2009). This seasonal
431 pattern is shown in the first LLC270R mode and second LLC270C mode.

432 The first and second EOF modes for AZ, MR, and CO with daily runoff forcing in coarse (LLC90R)
433 and fine (LLC540R) grid resolution are shown in Figures 7 and S5. The plume-like features and
434 associated dynamics are similar to LLC270 in both runs. Additionally, the higher-resolution LLC540R
435 resolves fine-scale plume structure for several major rivers, which was previously revealed by satellite
436 observations, regional simulations, or neural network methods (e.g. meanders and rings of the AZ plume
437 due to the North Brazilian Current (NBC) retroflection, Molleri *et al.* 2010). In LLC540R, “horseshoe”
438 patterns of the MR plume are associated with Texas floods (Fournier *et al.* 2016), and the bidirectional
439 CO plume is seen during variable summer wind patterns (Liu *et al.* 2009). Overall, EOF SSS analysis

440 shows that general plume patterns and dynamics are grid independent; however, fine-scale plume
 441 structures are only resolved by high-resolution simulations.

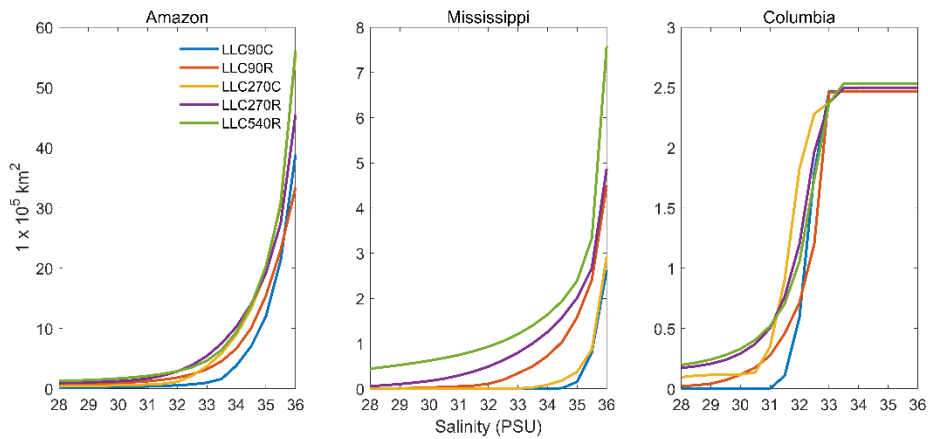


442 **Figure 7:** Same as Fig. 6 but for the LLC90R and LLC540R simulations. The corresponding PC
 443 timeseries are normalized by the standard deviation and multiplied with the spatial mode shown in Figure
 444 S5.
 445

446 **4.2 Plume Area, Volume, and Freshwater Thickness**

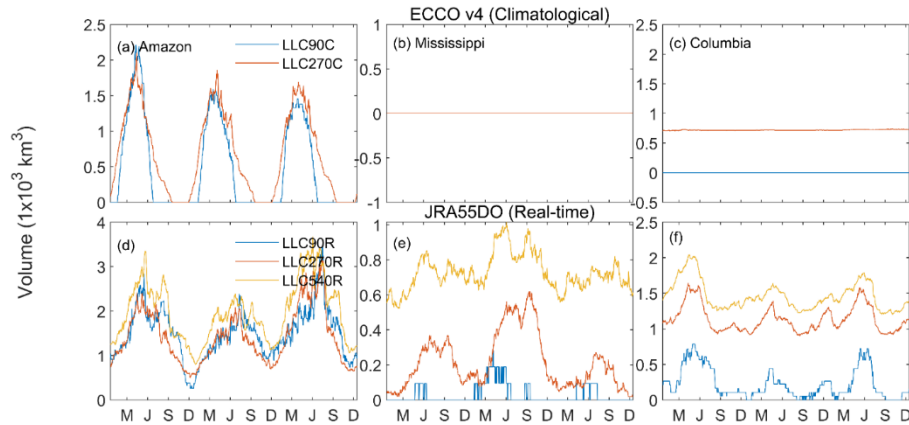
447 We first calculated the plume area using the salinity threshold from 28 to 36 PSU. The 3yr-average
 448 plume area for AZ, MR, and CO river region for different LLC configurations is shown in Figure 8.
 449 Under either the climatological diffusive or DPR river forcing, we could see the plume area increasing
 450 when model resolution increase from 1° to $1/3^\circ$ for all regions. While the plume area responds to the
 451 model resolution change to $1/6^\circ$, this can only can be seen in the Mississippi River region. To highlight
 452 the seasonal and interannual variability are at the given threshold, we also show the plume area and
 453 volume within $S_A = 30$ PSU using climatological and daily runoff forcing in the coarse-, intermediate-,
 454 and high- resolution runs (Figures S6, 9). Figure 9 presents a time series of freshwater volume within the
 455 given salinity during this period. There is a stronger interannual variability when using DPR, and larger
 456 plume area and volume during flood years. The MR and CO plume area/volume cannot be explicitly
 457 resolved at the $S_A = 30$ threshold when using the climatological and runoff forcing, since river runoff

458 has been distributed over broad spatial grids and surface salinity decrease is small. For the AZ region,
 459 the averaged plume area (volume) approaches $6 \times 10^4 \text{ km}^2$ ($7 \times 10^2 \text{ km}^3$) in LLC270C, whereas it is
 460 only about $3 \times 10^4 \text{ km}^2$ ($5 \times 10^2 \text{ km}^3$) in LLC90C. In contrast, the MR and CO plume area (volume) is
 461 easily recognized when using DPR forcing. The AZ plume increases as the grid resolution increases,
 462 reaching 10 , 13 , and $17 \times 10^4 \text{ km}^2$ in LLC90R, LLC270R, and LLC540R, respectively. The freshwater
 463 volume in coarse-, intermediate-, and high-resolution runs is comparable, with values of $\sim 1.5 - 2 \times 10^2$
 464 km^3 . The plume area and volume in the MR region is more sensitive to the model grid resolution than
 465 AZ and CO. The LLC540R plume area is $\sim 3-4$ times larger than LLC270R, while LLC270R is $\sim 6-7$
 466 times larger than LLC90R. When using DPR forcing, the CO region's plume area is similar between
 467 intermediate- and fine-resolution experiments, with the area in LLC270R and LLC540R increasing to ~ 1
 468 $\times 10^5 \text{ km}^2$ during the 2015 flood year. In contrast, LLC540R maintains a larger plume volume than the
 469 intermediate resolution run.



470
 471 **Figure 8:** 2015-2017 averaged plume area at salinity threshold S_a from 28 to 36 for the Amazon,
 472 Mississippi, and Columbia River regions.

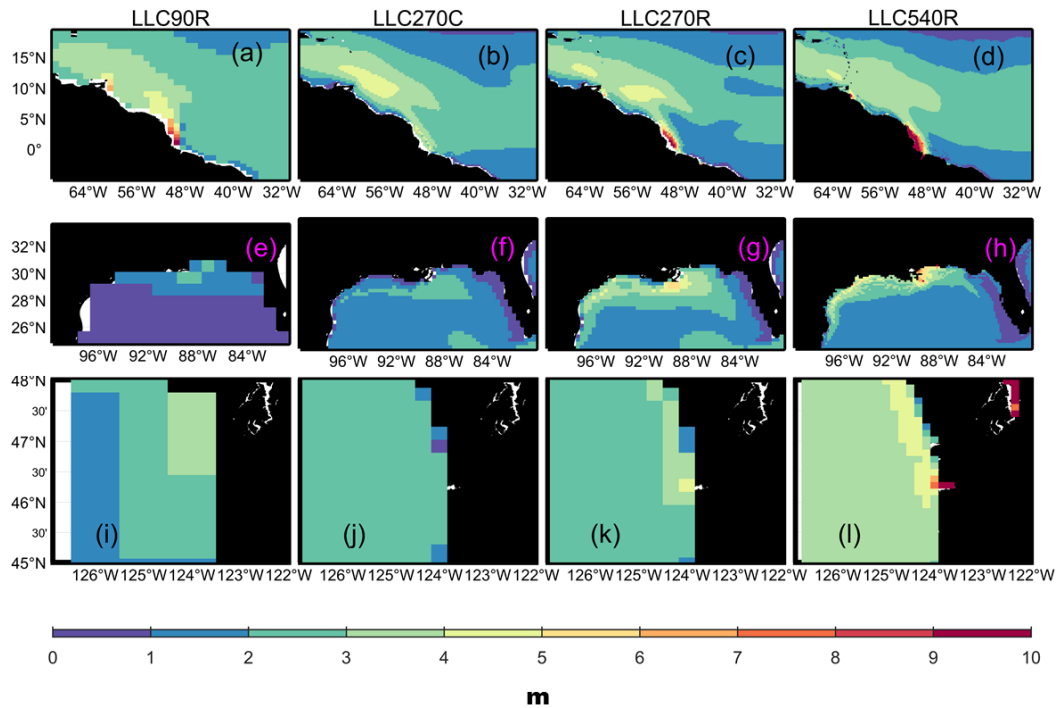
473



474
 475 **Figure 9:** Freshwater volume within 30 PSU for the Amazon, Mississippi, and Columbia river regions
 476 for various experiments; reference salinity is 36 PSU.

477 The sensitivity of plume area and volume to runoff forcing and grid resolution reflects the
 478 experiment’s ability to resolve horizontal advection and downward mixing of riverine freshwater. This
 479 can be partially reflected in the freshwater thickness calculation, which is shown in Figure 10. For the
 480 intermediate resolution experiments, the maximum freshwater thickness δ_{fw} is over 10 m, 5 m, and 4 m
 481 near the AZ, MR, and CO river mouths when using DPR, as opposed to 4 m, 2 m, and 2 m, when using
 482 climatological runoff. Additionally, the freshwater thickness in experiments with DPR but different grid
 483 resolutions (LLC270R and LLC540R) demonstrates that a coherent plume rotates and responds to
 484 external wind and background flow; this coastal plume structure is largely absent in the coarser LLC90R.
 485 The coarse-resolution experiment exhibits a more diffuse response, with lower salinity near MR and CO
 486 river mouths. Note that the runoff forcing is identical between LLC90R, LLC270R, and LLC540R
 487 experiments, and differences in plume area, volume, and freshwater thickness are due to model resolution
 488 alone. The freshwater flux in the higher resolution experiments can result in larger inflow velocities, a
 489 more robust baroclinic response, and a more vigorous coastal plume. The plume area and volume in MR
 490 region are more sensitive to grid resolution — this possibly results from the representation of shelf
 491 bathymetry. The Texas-Louisiana shelf is wider and shoals more gradually from the coastline than the

492 northern Brazilian shelf (AZ) and Washington shelf (CO). When adding the same amount of freshwater
 493 in shallow water regions, high resolution experiments generate a larger pressure gradient force than the
 494 intermediate resolution, which drive more substantial baroclinic effect and elevate coastal currents. The
 495 alongshore currents can advect the MR Plume water downcoast, which enlarges the plume area.
 496 Additionally, plume waters may be entrained downward by strong sub-grid vertical mixing and
 497 adjustment, e.g., meso-scale eddies, when flowing offshore to the open ocean as the horizontal resolution
 498 increases from intermediate to high. The eddies in high resolution run at AZ and CO may also break up
 499 the plumes and reduce their area compared to low-to-intermediate resolution runs (Figure 8).



500

501 **Figure 10:** Freshwater thickness for the Amazon, Mississippi, and Columbia river regions in LLC90R,
 502 LLC270C, LLC270R, and LLC540R experiments.

503 **4.3 Impact on Ocean Properties Associated with SSS**

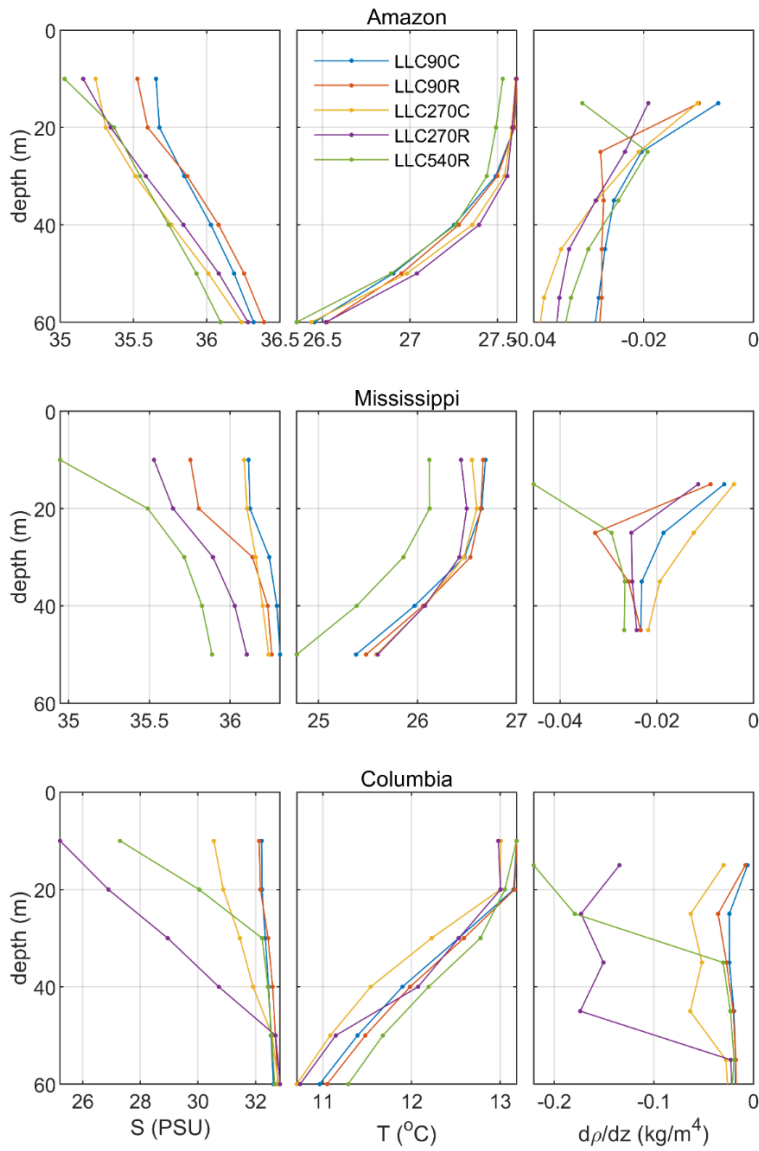
504 This section examines the sensitivity of stratification and mixed layer depth (MLD) between
 505 different experiments. Figure 11 shows 3-year averaged vertical profiles of salinity, temperature, vertical

506 density gradient $d\rho/dz$ (ρ is the potential density) near the AZ (top), MR (middle), and CO (bottom)
507 river mouths, respectively. The profiles are averaged over the horizontal regions shown in Figure S3.
508 The vertical density gradient is an important indicator of stratification strength. The salinity differences
509 between climatological (LLC90/270C) and DPR forcing (LLC90/270R) are large near the surface and
510 diminish with increasing depth. The temperature difference when using the two types of runoff forcing
511 is insignificant, demonstrating that the stratification difference is primarily determined by salinity and
512 the addition of freshwater. Additionally, DPR forcing greatly increases subsurface stratification, which
513 implies a decrease in vertical mixing.

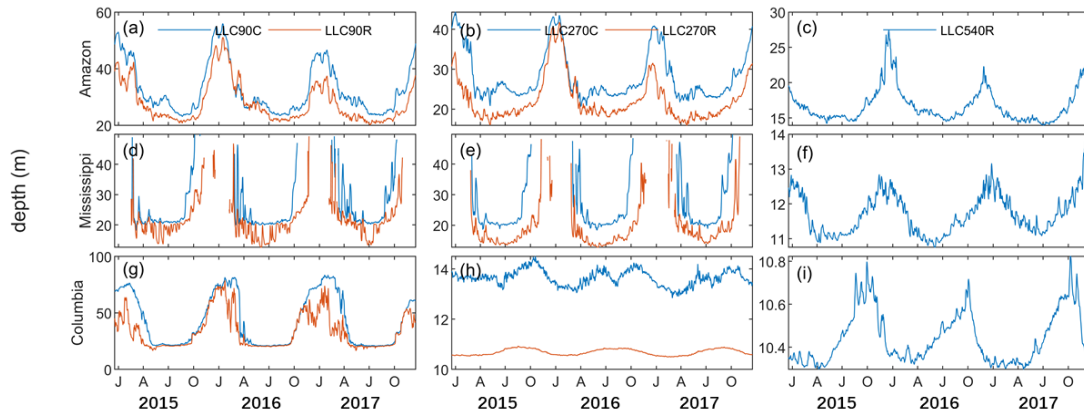
514 Figure 11 also shows the sensitivity of upper-ocean stratification to various model grid resolutions.
515 The profiles show a significant decrease in salinity from the surface to 50-m depth as the resolution
516 increases, impacting the stratification (rightmost panels). We note that the vertical density gradient has a
517 subsurface maximum in the coarse- and intermediate-resolution run. In contrast, the high-resolution
518 experiment has a surface maximum due to low-salinity water concentrated in the surface level. SST is
519 highest in LL540R at AZ and MR, reflecting that heat is preserved at the surface due to the increase in
520 subsurface stratification.

521 The sensitivity of stratification in the above analysis implies that the MLD can be altered by river
522 forcing and grid resolution. We compare the MLD in the vicinity of AZ, MR, and CO during the
523 simulation period in Figure 12. The MLD in our calculation uses the threshold method, in which deeper
524 levels are examined until one is found with a density differing from the near surface by more than 0.03
525 kg/m^3 (de Boyer Montégut et al., 2004). This reflects the maximum depth of the boundary layer that is
526 sustained by riverine freshwater. Interestingly, all experiments simulate the annual cycle of MLD. There
527 was relatively shallow MLD from April to December, which corresponds to periods of high river

528 discharge. The MLD in the DPR forcing and high-resolution scenario is shallower than the climatological,
 529 low-resolution scenario, which is consistent with vertical salinity and stratification profiles shown in
 530 Figure 11.



531
 532 **Figure 11:** Mean 3-year (2015-2017) salinity, potential temperature, and vertical density gradient
 533 ($d\rho/dz$) profiles.



534

535 **Figure 12.** 2015–2017 daily MLD, averaged in the vicinity of the Amazon River (upper panels),
 536 Mississippi River (middle panels), and Columbia River (lower panels) mouth. MLD is computed as done
 537 in Boyer Montegut et al. (2004).

538 **5. Discussion and conclusions**

539 This study investigates the model sensitivity of runoff forcing and grid resolution and type under the
 540 ECCO framework. We find that DPR significantly improves model representation of global rivers, with
 541 horizontal model resolution having a substantial control on SSS in the vicinity of river mouths. We
 542 observe no significant changes in tropical and temperate river mouth SSS when using cube sphere grid
 543 vs LLC grid types when using the same river forcing. A comparison with synchronized SMAP
 544 observations shows that the use of DPR forcing and intermediate grid resolution can increase the model
 545 performance in simulating SSS in the vicinity of river mouths. However, further increasing model grid
 546 resolution from intermediate to high may result in an additional SSS bias towards fresher values.

547 Previous theoretical modelling studies have demonstrated that, in the absence of external forcing,
 548 large river plumes influenced by rotational effects tend to veer anticyclonically and form a bulge region
 549 near the river mouth as well as an along-shore downstream coastal current as Kelvin waves (Kourafalou
 550 et al. 1996; Yankovsky and Chapman, 1997). Additionally, idealized numerical simulations have
 551 revealed that river plume behaviour is greatly impacted by external forcing. Chao (1988a, b)
 552 demonstrated that vertical mixing, bottom drag, and bottom slope greatly impact the spin-up,

553 maintenance, and dissipation of river plumes. Fong and Geyer (2001) revealed that a surface-trapped
554 river plume would thin and be advected offshore by cross-shore Ekman transport. Additionally, Fong
555 and Geyer (2002) suggested that the ambient current, which is in the same direction as the geostrophic
556 coastal current, can augment plume transport. Our ECCO experiments examine the above river plume
557 theoretical results globally with realistic topography and external atmospheric forcing. Our EOF analysis
558 of SSS at the AZ, MR, and CO shelves shows that the general plume spatial and temporal patterns related
559 to river discharge, wind, and currents are independent of the grid resolution and forcing formulations,
560 which are consistent with previous theoretical studies. However, higher resolution and DPR forcing may
561 be vital for resolving the small rivers' fine-scale plume dynamics. Using DPR forcing and increasing the
562 model grid resolution from coarse to intermediate increases the river plume area and volume, while
563 further increasing the model resolution from intermediate to high has mostly regional effects. Shallow
564 and wide shelf regions, such as the Mississippi Delta, are more sensitive to the model resolution
565 compared to AZ and CO. Recent increases in computational power have allowed GODAS products, such
566 as ECCO, to provide model output at different resolutions, which supports regional scientific studies
567 using offline methods (e.g. the Lagrangian method, Meng et al. 2020; Liang et al. 2019). Our results
568 suggest that how high-resolution products should be used depends on the relevant spatio-temporal
569 dynamics and geomorphologic characteristic of the studied region. We also found that using DPR forcing
570 and increasing the model grid resolution can stabilize the water column at the subsurface and shoal the
571 MLD. This may have significant implications for biogeochemical cycles and air-sea exchange in coastal
572 zones. From the biogeochemistry perspective, riverine freshwater increases shelf stratification, which
573 can prevent reoxygenation of bottom waters and thus can result in large hypoxic regions (Fennel, et al.
574 2011; Feng et al. 2019). From the air-sea interaction perspective, on one hand, SST can trigger deep

575 atmospheric convection and intense rainfall. On the other hand, strong near-surface stratification may
576 inhibit cooling and intensify tropical cyclones (Cione and Uhlhorn, 2003; Neetu et al., 2012; Rao and
577 Sivakumar, 2003; Sengupta et al., 2008; Vialard & Allison et al., 2000; Vinaychandran et al., 2002). We
578 envision that future work investigating river impacts on ocean-atmospheric and earth system dynamics
579 could be accomplished by coupling our improved ECCO simulations with an atmospheric general
580 circulation model (AGCM).

581 In the state-of-art OGCMs, ESMs, and most GODAS products, river runoff is incorporated on coarse
582 resolution grids as augmented precipitation. Climatological runoff forcing is often used in conjunction
583 with artificial spreading and a virtual salt flux scheme. Tseng et al. (2016) examined model sensitivity to
584 the spreading radius, turbulent mixing parameterization, reference salinity, and vertical distribution of
585 riverine freshwater on 1° resolution in Community Earth System Model (CESM). For all factors
586 examined, they found that the model results are most sensitive to the spreading radius, which
587 substantiates the importance of our finding that the associated plume properties, including the area hence
588 the SSS near river mouths exhibit strong responses when switching the runoff flux from diffusive
589 climatological to daily point-source.

590 The present state-of-the art regional scale estuarine models can simulate estuarine hydrodynamics
591 and biogeochemical processes in a robust manner. The inlet approach, which defines a rectangular breach
592 in coastal land cells with uniform density and discharge, is widely used (Herzfeld, 2015; Garvine, 2001).
593 An additional barotropic pressure term may be added to account for pressure gradients induced by the
594 freshwater plume (Schiller and Kourafalou, 2011). The inlet approach has also been used in global z-
595 coordinate models by injecting freshwater in multiple vertical grid cells (Griffies et al. 2005). In our
596 simulations, sea level changes are redistributed over-all vertical grid cells by the rescaled height vertical

597 coordinate. This is similar to the inlet approach in the regional models, which add a mass or volume flux
598 of freshwater to a breach in coastal land cells (Garvine 1999). Herzfeld (2015) investigated the role of
599 model resolution on plume response at the Great Barrier Reef (GBR) using the Regional Ocean Modeling
600 System (ROMS). The study found that the plume veered left and followed a northward trajectory to Cape
601 Bowling Green in a 1 km resolution model but not in a 4 km resolution model. Our findings are consistent
602 with this result. The plume properties in our intermediate resolution simulations are more clearly detected
603 than in the coarse resolution simulations. Our results also expand on their findings by showing that the
604 sensitivity of plume properties in high resolution model is highly-dependent on shelf bathymetry. Schiller
605 and Kourafalou (2010) investigated the dynamics of large-scale river plumes in idealized numerical
606 experiments using HYCOM to address how the development and structure of a buoyant plume are
607 affected by the vertical and horizontal redistribution of river inflow and bottom topography. Their
608 experiments show that a narrow inlet, flat bottom facilitates a larger right-turning plume bulge region
609 than a wide inlet, slope bottom (see their Figure 8 Riv2c-f; Riv2c-s). This is complementary to our
610 findings that the MR plume, located on the wide and shallow LA shelf, has a larger horizontal plume
611 area than the AZ and CO plume when increasing the horizontal resolution from intermediate to high.
612 However, their discussion was limited to an idealized, rectangular model domain without external forcing,
613 while our model simulations provide a practical application to natural river plume systems. The global
614 application of the regional inlet representation of river forcing was also used by NOAA's Geophysical
615 Fluid Dynamics Laboratory (GFDL) models (Griffies et al., 2005). An internal, pre-computed salinity
616 source term was introduced into multiple vertical layers. However, river representation was done through
617 virtual salt flux rather than through real mass or freshwater volume flux. Adding the real volume and
618 mass of freshwater through multiple layers has been widely used in regional models like ROMS; it may

619 be useful to adapt this technology into future ECCO simulations and compare the results with the current
620 surface injection methods.

621 For the global ocean, river runoff is much smaller than the precipitation and evaporation flux;
622 therefore, it is parameterized for most OGCMs, ESMs, and GODAS products. One of the most significant
623 expected signatures of global warming is an acceleration of the terrestrial hydrological cycle (IPCCs,
624 2019; Piecuch and Wadehra, 2020). Both can significantly affect the magnitude, distribution, and timing
625 of global runoff, leading to extremes in the frequency and magnitude of floods and droughts. When
626 considering water resource management issues under climate and land use/land cover change, a key
627 question such as “how will coastal oceans be impacted from flood and drought events?” is challenging
628 to answer (Fournier et al., 2019). In the future, high-resolution global-ocean circulation models with DPR
629 forcing may help identify the primary forcing mechanisms, such as those from climate-driven extreme
630 events, which drive variability of large river plume systems just as skillfully as a regional model set-up.

631 Improved model representation of rivers may not be as important for global or basin- scale
632 hydrological cycles as precipitation and evaporation (Du and Zhang, 2015), but may be critical for the
633 global carbon cycle (Friedlingstein et al., 2019; Resplandy et al. 2018). River delivers large amounts of
634 anthropogenic nutrients to the coastal zone (Seitzinger et al., 2005, 2010). The autochthonous production
635 will transform inorganic nutrients to organic while sequestering atmospheric CO₂. More importantly,
636 rivers also deliver dissolved organic carbon (DOC) and particulate organic carbon (POC) to the coastal
637 ocean, which can be remineralized and released as CO₂ to the atmosphere. Until recently, most global-
638 ocean biogeochemistry models omitted or poorly represented riverine point sources of nutrients and
639 carbon. Lacroix et al. (2020) added yearly-constant riverine loads to the ocean surface layer on a coarse
640 resolution (1.5°) model. They assessed that CO₂ outgassing from river loads accounted for ~10% of the

641 global ocean CO₂ sink. We anticipate that the implementation of DPR forcing and higher-resolution grids
642 in ESMs and ECCO biogeochemical state estimates (ECCO-Darwin, Carroll et al., 2020) will help better
643 resolve the global carbon budget (Friedlingstein et al., 2019).

644 LOAC development has historically had a low priority in OGCMs, ESMs, and GODAPs, and the
645 exchange of freshwater between rivers/estuaries and the coastal ocean has been previously neglected.
646 Our results demonstrate that the representation of runoff forcing in ECCO simulations is a major source
647 of bias for coastal SSS. Our improvements and sensitivity analysis of river runoff in ECCO will directly
648 contribute to: (i) the evaluation, understanding, and improvement of river-dominated coastal margins in
649 global-ocean circulation models, (ii) investigation of mechanisms that drive seasonal and interannual
650 variability in coastal plume processes, and (iii) bridge the gap between land-ocean interactions. These
651 efforts will ultimately help to resolve land-ocean-atmosphere processes and feedbacks in next-generation
652 earth system models better.

653

654 **Code and Data Availability**

655 The MITgcm and user manual are available from the project website: <http://mitgcm.org/>. The ECCOv4
656 setup can be found at http://wwwcvs.mitgcm.org/viewvc/MITgcm/MITgcm_contrib/lle_hires/. The
657 exact version of MITgcm, ECCOv4 configuration, MATLAB routines to process the ECCOv4 output,
658 generate the target model skill assessment diagram, and produce the paper figures are archived on Zenodo
659 (doi:10.5281/zenodo.4106405). The SMAP observations can be downloaded from
660 <http://apdrc.soest.hawaii.edu/las/v6/dataset?catitem=2928>. The model forcing and simulated salinity
661 fields at different resolutions are archived on Zenodo (doi:10.5281/zenodo.4095613).

662

663 **Author Contribution**

664 Dimitris Menemenlis designed the experiments and Hong Zhang carried them out. Dimitris Menemenlis,
665 Hong Zhang, Dustin Carroll, and Yang Feng developed the model code. Yang Feng prepared the
666 manuscript with contributions from Huijie Xue, Dustin Carrol, Yan Du, and Hui Wu.

667

668 **Acknowledgment**

669 The work was supported by CAS Pioneer Hundred Talents Program Startup Fund (Y9SL11001);
670 Southern Marine Science and Engineering Guangdong Laboratory (Guangzhou) (GML2019ZD0303,
671 2019BT2H594), ISEE2018PY05 from Chinese Academy of Sciences; the Chinese Academy of
672 Sciences (XDA15020901; 133244KYSB20190031), the National Natural Science Foundation of China
673 (41830538 and 42090042), and Guangdong Key Laboratory of Ocean Remote Sensing (South China
674 Sea Institute of Oceanology Chinese Academy of Sciences) (2017B030301005-LORS2001). D.M.,
675 D.C., and H.Z., carried out research at Jet Propulsion Laboratory, California Institute of Technology,
676 under contract with NASA, with grants from Biological Diversity, Physical Oceanography, and
677 Modeling, Analysis, and Prediction Programs.

678

679

680 **References**

- 681 Adcroft, A., and Campin, J.-M., Rescaled height coordinates for accurate representation of free-surface
682 flows in ocean circulation models, *Ocean Modelling*, 7(3), 269-284,
683 doi:10.1016/j.ocemod.2003.09.003, 2004
- 684 Adcroft, A., Campin, J.-M. Hill, C. and Marshall, J., Implementation of an Atmosphere–Ocean General
685 Circulation Model on the Expanded Spherical Cube, *Monthly Weather Review*, 132(12), 2845-2863,
686 doi:10.1175/MWR2823.1, 2004
- 687 Banas, N. S., MacCready, P. and Hickey, B. M., The Columbia River plume as cross-shelf exporter and
688 along-coast barrier, *Continental Shelf Research*, 29(1), 292-301, doi:10.1016/j.csr.2008.03.011.,2009
- 689 Barichivich, J., Gloor, E., Peylin, P., Brienen, R. J. W., Schöngart, J., Espinoza, J. C., and Pattnayak,
690 K. C., Recent intensification of Amazon flooding extremes driven by strengthened Walker circulation,
691 *Science Advances*, 4(9), eaat8785, doi:10.1126/sciadv.aat8785.,2018
- 692 Bentsen, M., The Norwegian Earth System Model, NorESM1-M - Part 1: Description and basic
693 evaluation of the physical climate, *Geoscientific. Model Development*, 6, 687-720, doi:10.5194/gmd-6-
694 687-2013.,2013

695 Bourgeois, T., Resplandy, J. C. Orr, L., Terhaar, J., Ethé, C., Gehlen, M. and Bopp, L., Coastal-ocean
696 uptake of anthropogenic carbon, *Biogeosciences*, 13(14), 4167-4185, doi:10.5194/bg-13-4167-
697 2016.,2016

698 Campin, J.-M., Marshall, J. and Ferreira, D., Sea ice–ocean coupling using a rescaled vertical
699 coordinate z^* , *Ocean Modelling*, 24, 1-14, doi:10.1016/j.ocemod.2008.05.005., 2008

700 Carroll, D., Menemenlis, Adkins, J.F., Bowman, K.W., Brix, H., Dutkiewicz, S., Gierach, M. M., Hill,
701 C., Jahn, O., Landschützer, P., Lauderdale, J. Liu, J.M., Naviaux, J.D., Manizza, M., Rödenbeck,
702 C., Schimel, D. S., Van der Stocken, T., and Zhang, (2020) H, Seasonal to Multi-decadal Air-sea CO₂
703 Fluxes from the Data-constrained ECCO-Darwin Global Ocean Biogeochemistry Model, *Journal of*
704 *Advances in Modeling Earth Systems*, Accepted

705 Chao, S. -Y., River-forced estuarine plumes. *Journal of Physical Oceanography.*, 18, 72 – 88.
706 [doi:10.1175/1520-0485\(1988\)018<0072:RFEP>2.0.CO;2](https://doi.org/10.1175/1520-0485(1988)018<0072:RFEP>2.0.CO;2), 1988

707 Chao, S. -Y., Wind-driven motion of estuarine plumes, *Journal of Physical Oceanography*, 18, 1144-
708 1166. doi:10.1175/1520-0485(1988)018<1144:WDMOEP>2.0.CO;2; 1988

709 Cione, J. J., and Uhlhorn, E. W. Sea surface temperature variability in hurricanes: Implications with
710 respect to intensity change. *Monthly Weather Review*. 1783-1796, doi:10.1175/2562.1; 2003

711 Cochrane, J. D., Kelly, F. J., Low-frequency circulation on the Texas-Louisiana continental shelf. *J.*
712 *Geophys. Res.* 91(C9), 10645-10659.,1986

713 de Boyer Montégut, C., Madec, G., Fischer, A. S., Lazar, A. & Ludicone, D, Mixed layer depth over
714 the global ocean: An examination of profile data and a profile-based climatology, 109(C12),
715 doi:10.1029/2004jc002378.,2004

716 Denamiel, C., Budgell, W. P. & Toumi, R, The Congo River plume: Impact of the forcing on the far-
717 field and near-field dynamics, *Journal of Geophysical Research-Oceans*, 118, 964–989,
718 doi:10.1002/jgrc.20062.,2013

719 Du, Y., & Zhang, Y., Satellite and Argo Observed Surface Salinity Variations in the Tropical Indian
720 Ocean and Their Association with the Indian Ocean Dipole Mode. *J. Climate*, 28, 695–713,
721 doi:10.1175/JCLI-D-14-00435.1.,2015

722 Fekete, B. M., Vörösmarty, C. J. and Grabs, W, High-resolution fields of global runoff combining
723 observed river discharge and simulated water balances, 16(3), 15-11-15-10,
724 doi:10.1029/1999gb001254.,2002

725 Fennel, K., et al. Carbon cycling in the North American coastal ocean: a synthesis, *Biogeosciences*,
726 16(6), 1281-1304, doi:10.5194/bg-16-1281-2019.,2019

727 Fennel, K., Hu, J., Laurent, A., Marta-Almeida, M., & Hetland, R. Sensitivity of hypoxia predictions
728 for the northern Gulf of Mexico to sediment oxygen consumption and model nesting. *Journal of*
729 *Geophysical Research: Oceans*, 118, 990–1002. doi:10.1002/jgrc.20077., 2013

730 Feng, Y., DiMarco, S. F., Balaguru, K., and Xue, H. Seasonal and interannual variability of areal extent
731 of the Gulf of Mexico hypoxia from a coupled physical-biogeochemical model: A new implication for
732 management practice. *Journal of Geophysical Research: Biogeosciences*, 124,1939–1960.
733 doi:10.1029/2018JG004745.,2019

734 Fong, D. A., and Geyer, W. R., Response of a river plume during an upwelling favorable wind event,
735 *Journal of Geophysical Research-Oceans*, 106(C1), 1067-1084, doi:10.1029/2000jc900134., 2001

736 Fong, D. A., and Geyer, W. R., The Alongshore Transport of Freshwater in a Surface-Trapped River
737 Plume, *Journal of Physical Oceanography*, 32(3), 957-972, doi:10.1175/1520-
738 0485(2002)032<0957:TATOFI>2.0.CO;2, 2002

739 Forget, G., Campin, J. M., Heimbach, P., Hill, C. N., Ponte, R. M. and Wunsch, C., ECCO version 4:
740 an integrated framework for non-linear inverse modeling and global ocean state estimation,
741 *Geoscientific Model Development*, 8(10), 3071-3104, doi:10.5194/gmd-8-3071-2015, 2015

742 Fournier, S., Reager, J. T., Lee, T., Vazquez-Cuervo, J., David, C.H., and Gierach, M. M., SMAP
743 observes flooding from land to sea: The Texas event of 2015, *Geophysical Research Letter*, 43,
744 L070821, doi:10.1002/2016GL070821, 2016

745 Fournier, S., Lee, T. and Gierach, M. M., Seasonal and interannual variations of sea surface salinity
746 associated with the Mississippi River plume observed by SMOS and Aquarius, *Remote Sensing of*
747 *Environment*, 180, 431 – 439. doi:10.1016/j.rse.2016.02.050, 2016

748 Fournier, S., Vialard, J., Lengaigne, M., Lee, T., Gierach, M. M., and Chaitanya, A. V. S. Modulation
749 of the Ganges-Brahmaputra river plume by the Indian Ocean dipole and eddies inferred from satellite
750 observations. *Journal of Geophysical Research: Oceans*, 122, 9591–9604. doi:10.1002/2017JC013333,
751 2017

752 Fournier, S., Vandemark, D., Gaultier, L., Lee, T., Jonsson, B., and Gierach, M. M. Interannual
753 variation in offshore advection of Amazon-Orinoco plume waters: Observations, forcing mechanisms,
754 and impacts. *Journal of Geophysical Research: Oceans*, 122, 8966–8982. doi:10.1002/2017JC013103,
755 2017

756 Fournier, S., Reager, J. T., Dzwonkowski, B., and Vazquez-Cuervo, J. Statistical mapping of
757 freshwater origin and fate signatures as land/ocean “regions of influence” in the Gulf of Mexico.
758 *Journal of Geophysical Research: Oceans*, 124, 4954–4973. doi:10.1029/2018JC014784, 2019

759 Friedlingstein, P., et al., Global Carbon Budget 2019, *Earth System Science Data*, 11, 1783-1838,
760 doi:10.5194/essd-11-1783-2019., 2019

- 761 García Berdeal, I., B. M. Hickey, and M. Kawase, Influence of wind stress and ambient flow on a high
762 discharge river plume, 107(C9), 13-11-13-24, doi:10.1029/2001jc000932.,2002
- 763 Garvine, R.W., Penetration of buoyant coastal discharge onto the continental shelf: a numerical model
764 experiment. *Journal of Physical. Oceanography.* 29, 1892–1909. doi:10.1175/1520-
765 0485(1999)029<1892:POBCDO>2.0.CO;2,1999
- 766 Garvine, R. W. The impact of model configuration in studies of buoyant coastal discharge. *Journal of*
767 *Marine Research.* 59, 193-225. doi:10.1357/002224001762882637, 2001
- 768 Gaspar, P., Grégoris, Y. & Lefevre, J.-M., A simple eddy kinetic energy model for simulations of the
769 oceanic vertical mixing: Tests at station Papa and long-term upper ocean study site, 95(C9), 16179-
770 16193, doi:10.1029/JC095iC09p16179, 1990
- 771 Gent, P. and McWilliams, J.: Isopycnal mixing in ocean circulation models, *J. Phys. Oceanogr.*, 20,
772 150–155, 1990.
- 773 Gierach, M. M., Vazquez-Cuervo, J., Lee, T., and Tsontos, V. M., Aquarius and SMOS detect effects
774 of an extreme Mississippi River flooding event in the Gulf of Mexico, *Geophysical Research Letter*,
775 40, L50995. doi:10.1002/grl.50995, 2013
- 776 Griffies, S. M., et al., Formulation of an ocean model for global climate simulations, *Ocean Science*,
777 1(1), 45-79, doi:10.5194/os-1-45-2005. 2005
- 778 Griffies, S. M., Gnanadesikan, A. Pacanowski, R. C., Larichev, V. D., Dukowicz, J. K. and Smith, R.D.
779 Isonutral Diffusion in a z-Coordinate Ocean Model, *Journal of Physical Oceanography* 28, 5 (1998):
780 805-830, doi:10.1175/1520-0485(1998)028<0805:IDIAZC>2.0.CO;2, 1998
- 781 Halliwell, G. R., Evaluation of vertical coordinate and vertical mixing algorithms in the HYbrid-
782 Coordinate Ocean Model (HYCOM), *Ocean Modelling*, 7(3), 285-322,
783 doi:10.1016/j.ocemod.2003.10.002.,2004
- 784 Herzfeld, M., Methods for freshwater riverine input into regional ocean models, *Ocean Modelling*, 90,
785 1-15, doi:10.1016/j.ocemod.2015.04.001.,2015
- 786 Huang, R. X., Real Freshwater Flux as a Natural Boundary Condition for the Salinity Balance and
787 Thermohaline Circulation Forced by Evaporation and Precipitation, *Journal of Physical Oceanography*,
788 23(11), 2428-2446, doi:10.1175/1520-0485(1993)023<2428:RFFAAN>2.0.CO;2, 1993
- 789 Kourafalou, V. H., Oey, L.-Y., Wang, J. D., and Lee, T. N., The fate of river discharge on the
790 continental shelf: 1. Modeling the river plume and the inner shelf coastal current, *Journal of*
791 *Geophysical Research*, 101(C2), 3415– 3434, doi:10.1029/95JC03024.,1996

792 IPCCs, Climate Change and Land: an IPCC special report on climate change, desertification, land
793 degradation, sustainable land management, food security, and greenhouse gas fluxes in terrestrial
794 ecosystems [P.R. Shukla, J. Skea, E. Calvo Buendia, V. Masson-Delmotte, H.-O. Pörtner, D. C.
795 Roberts, P. Zhai, R. Slade, S. Connors, R. van Diemen, M. Ferrat, E. Haughey, S. Luz, S. Neogi, M.
796 Pathak, J. Petzold, J. Portugal Pereira, P. Vyas, E. Huntley, K. Kissick, M. Belkacemi, J. Malley,
797 (eds.)]. In press. 2019

798 Jolliff, J. K., Kindle, J. C., Shulman, I., Penta, B., Friedrichs, M. A. M., Helber, R. and Arnone, R. A.,
799 Summary diagrams for coupled hydrodynamic-ecosystem model skill assessment, *Journal of Marine*
800 *Systems*, 76(1), 64-82, doi:10.1016/j.jmarsys.2008.05.014., 2009

801 Lacroix, F., Ilyina, T. and Hartmann, J., Oceanic CO₂ outgassing and biological production hotspots
802 induced by pre-industrial river loads of nutrients and carbon in a global modeling approach,
803 *Biogeosciences*, 17(1), 55-88, doi:10.5194/bg-17-55-2020.,2020

804 Landschützer, P., Gruber, N. and Bakker, D. C. E., Decadal variations and trends of the global ocean
805 carbon sink, *Global Biogeochemical Cycles*, 30(10), 1396-1417, doi:10.1002/2015GB005359.,2016

806 Landschützer, P., Laruelle, G. G., Roobaert, A., and Regnier, P.: A uniform pCO₂ climatology
807 combining open and coastal oceans, *Earth Syst. Sci. Data Discuss.*, doi: 10.5194/essd-2020-90, in
808 review, 2020

809 Lentz, S. J., The Amazon River plume during AMASSEDS: subtidal current variability and the
810 importance of wind forcing. *Journal of Geophysical Research – Oceans*, 100, 2377–2390,
811 doi:10.1029/94JC00343, 1995a

812 Lentz, S. J., Seasonal variations in the horizontal structure of the Amazon plume inferred from
813 historical hydrographic data. *Journal of Geophysical Research-Oceans*, 100, 2391–2400,
814 doi:10.1029/94JC01847, 1995b

815 Liang, L., Xue, H., & Shu, Y. (2019). The Indonesian throughflow and the circulation in the Banda
816 Sea: A modeling study. *Journal of Geophysical Research: Oceans*, 124. doi:10.1029/2018JC014926

817 Liao, X., Du, Y., Wang, T., Hu, S., Zhan, H., Liu, H. and Wu, G., High-Frequency Variations in Pearl
818 River Plume Observed by Soil Moisture Active Passive Sea Surface Salinity, *Remote Sensing*, 12, 563,
819 doi:10.3390/rs12030563, 2020

820 Liu, Y., MacCready, P. and Hickey, B. M., Columbia River plume patterns in summer 2004 as revealed
821 by a hindcast coastal ocean circulation model, *Geophysical Research Letter*, 36, L02601,
822 doi:10.1029/2008GL036447.,2009

823 Marshall, J., Adcroft, A., Hill, C., Perelman, L. and Heisey, C., A finite-volume, incompressible Navier
824 Stokes model for studies of the ocean on parallel computers, 102(C3), 5753-5766,
825 doi:10.1029/96jc02775.,1997

- 826 Mecklenburg, S., Drusch, M., Kerr, Y. H., Font, J., Martin-Neira, M., Delwart, S., . . . Crapolicchio, R.
827 ESA's soil moisture and ocean salinity mission: Mission performance and operations. IEEE
828 Transactions on Geoscience and Remote Sensing, 50, 1354–1366.
829 Doi:10.1109/TGRS.2012.2187666.,2012
- 830 Menemenlis, D., Hill, C. N., Adcroft, A. J., Campin, J.-M., Cheng, B., Ciotti, R. B., . . . Zhang, J.
831 NASA Supercomputer Improves Prospects for Ocean Climate Research. EOS Transactions AGU 86,
832 89–96. Doi:10.1029/2005EO090002,2005
- 833 Menemenlis, D., Campin, J.-M., Heimbach, P., Hill, C. N., Lee, T., Nguyen, A. T., . . . Zhang, H.
834 ECCO2: High Resolution Global Ocean and Sea Ice Data Synthesis. Mercator Ocean Quarterly
835 Newsletter, 31, 13–21.,2008
- 836 Meng, Z., Ning, L. Yuping G., & Yang, F. Exchanges of surface plastic particles in the South China
837 Sea through straits using Lagrangian method, Journal of Tropical Oceanography, 39, 109-116.
838 doi:10.11978/2019118 (In Chinese with English Abstract)
- 839 Molleri, G.S.F., Novo, E. M. L. M. & Kampel, M. Space-time variability of the Amazon River plume
840 based on satellite ocean color, Continental Shelf Research, 30, 342-352. [doi:10.1016/j.csr.2009.11.015](https://doi.org/10.1016/j.csr.2009.11.015),
841 2010
- 842 Neetu, S., Lengaigne, M., Vincent, E. M., Vialard, J., Madec, G., Samson, G., . . . Durand, F. Influence
843 of upper-ocean stratification on tropical cyclones-induced surface cooling in the Bay of Bengal. Journal
844 of Geophysical Research-Oceans, 117, C12020, doi:10.1029/2012JC008433,2012
- 845 Palma, E. D., & Matano, R. P., An idealized study of near equatorial river plumes, J. Geophys. Res.
846 Oceans, 122, 3599–3620, doi:10.1002/2016JC012554, 2017
- 847 Picuch, C. G., & Wadehra, R. Dynamic sea level variability due to seasonal river discharge: A
848 preliminary global ocean model study. Geophysical Research Letters, 47, e2020GL086984.
849 Doi:10.1029/2020GL086984,2020
- 850 Rao, R. R., and Sivakumar, R. Seasonal variability of the salt budget of the mixed layer and near-
851 surface layer salinity structure of the tropical Indian Ocean from a new global ocean salinity
852 climatology. Journal of Geophysical Research-Oceans, 108, 3009. [doi:10.1029/2001JC000907](https://doi.org/10.1029/2001JC000907), 2003
- 853 Resplandy, L., Keeling, R.F., Rödenbeck, C., Stephens, B.B., Khatiwala, S., Rodgers, K.B., Long,
854 M.C., Bopp, L., Tans, P.P., Revision of global carbon fluxes based on a reassessment of oceanic and
855 riverine carbon transport. Nature Geoscience 1. doi: 10.1038/s41561-018-0151-3,2018
- 856 Roobaert, A., Laruelle, G. G. Landschützer, P., Gruber, N., Chou, L. and Regnier, P., The
857 Spatiotemporal Dynamics of the Sources and Sinks of CO₂ in the Global Coastal Ocean, Global
858 Biogeochemical Cycles, 33(12), 1693-1714, doi:10.1029/2019GB006239,2019

859 Rouillet, G., and Madec, G., Salt conservation, free surface, and varying levels: A new formulation for
860 ocean general circulation models, 105(C10), 23927-23942, doi:0.1029/2000jc900089.,2000

861 Santini, M., and Caporaso, L. Evaluation of freshwater flow from rivers to the sea in CMIP5
862 simulations: Insights from the Congo River basin. *Journal of Geophysical Research: Atmospheres*, 123,
863 10,278–10,300. Doi:10.1029/2017JD027422,2018

864 Schiller, R. V., and Kourafalou, V. H., Modeling river plume dynamics with the HYbrid Coordinate
865 Ocean Model, *Ocean Modelling*, 33(1), 101-117, doi:10.1016/j.ocemod.2009.12.005.,2011

866 Seitzinger, S. P., Harrison, J. A., Dumont, E., Beusen, A. H. W., and Bouwman, A. F., Sources and
867 delivery of carbon, nitrogen, and phosphorus to the coastal zone: An overview of Global Nutrient
868 Export from Watersheds (NEWS) models and their application, *Global Biogeochemical Cycles*, 19,
869 GB4S01, doi:10.1029/2005GB002606.,2005

870 Seitzinger, S. P., Mayorga, E., Bouwman, A. F., Kroeze, C., Beusen, A. H. W., Billen, G., Dreht, G.
871 V., Dumont, E., Fekete, B. M., Garnier, J., and Harrison, J. A. Global river nutrient export: A scenario
872 analysis of past and future trends, *Global Biogeochemical Cycles.*, 24, GB0A08,
873 doi:10.1029/2009GB003587.,2010

874 Sengupta, D., Goddalahundi, B. R., and Anitha, D. S. Cyclone-induced mixing does not cool SST in
875 the post-monsoon North Bay of Bengal. *Atmospheric Science Letters*, 9, 1–6.
876 Doi:10.1002/asl.162.,2008

877 Stammer, D., Ueyoshi, K., Köhl, A. Large, W.G., Josey, S. A., and Wunsch, C., Estimating air-sea
878 fluxes of heat, freshwater, and momentum through global ocean data assimilation, *Journal of*
879 *Geophysical Research*, 109(C5), doi:10.1029/2003jc002082.,2004

880 Su, Z., Wang, J., Klein, P., Thompson, A. F. and Menemenlis, D., Ocean sub mesoscales as a key
881 component of the global heat budget, *Nature Communications*, 9, 775, doi:10.1038/s41467-018-02983-
882 w.,2018

883 Suzuki, T., Yamazaki, D., Tsujino, H., Komuro, Y., Nakano, H., and Urakawa, S., A dataset of
884 continental river discharge based on JRA-55 for use in a global ocean circulation model, *Journal of*
885 *Oceanography*, 74(4), 421-429, doi:10.1007/s10872-017-0458-5.,2018

886 Timmermann, R., Danilov, S., Schröter, J., Böning, C., Sidorenko, D., and Rollenhagen, K., Ocean
887 circulation and sea ice distribution in a finite element global sea ice–ocean model, *Ocean Modelling*,
888 27(3), 114-129, doi:10.1016/j.ocemod.2008.10.009.2009

889 Tseng, Y.-h., Bryan, F. O. and Whitney, M. M., Impacts of the representation of riverine freshwater
890 input in the community earth system model, *Ocean Modelling*, 105, 71-86,
891 doi:10.1016/j.ocemod.2016.08.002.,2016

892 Tsujino, H., et al., JRA-55 based surface dataset for driving ocean–sea-ice models (JRA55-do), *Ocean*
893 *Modelling*, 130, 79-139, doi:10.1016/j.ocemod.2018.07.002.,2018

894 Volodin, E. M., Dianskii, N. A. and Gusev, A. V., Simulating present-day climate with the INMCM4.0
895 coupled model of the atmospheric and oceanic general circulations, *Izvestiya, Atmospheric and*
896 *Oceanic Physics*, 46(4), 414-431, doi:10.1134/S000143381004002X, 2010

897 Vialard, J., and Delecluse, P. An OGCM study for the TOGA decade. Part I: Role of salinity in the
898 physics of the western Pacific fresh pool. *Journal of Physical Oceanography*, 28, 1071–1088.
899 [doi:10.1175/1520-0485\(1998\)028<1071:AOSFTT>2.0.CO;2](https://doi.org/10.1175/1520-0485(1998)028<1071:AOSFTT>2.0.CO;2), 1998

900 Vinaychandran, P., Murty, V. S. N., and Ramesh Babu, V. Observations of barrier layer formation in
901 the Bay of Bengal during summer monsoon. *Journal of Geophysical Research-Oceans*, 107, 8018.
902 Doi:10.1029/2001JC000831,2002

903 Walker, N. D. Satellite assessment of Mississippi River plume variability: causes and predictability,
904 *Remote Sensing of Environment*, 58, 21-35. doi:10.1016/0034-4257(95)00259-6,1996

905 Ward, N.D., Megonigal, J.P., Bond-Lamberty, B. *et al.* Representing the function and sensitivity of
906 coastal interfaces in Earth system models. *Nature Communicaitons* **11**, 2458 (2020).
907 <https://doi.org/10.1038/s41467-020-16236-2>.

908 Willmott, C. J., On the validation of models, *Phys. Geogr.*, 2, 184–194,
909 doi:10.1080/02723646.1981.10642213.,1981

910 Yueh, S. H., Tang, W., Fore, A. G., Neumann, G., Hayashi, A., Freedman, A., . . . Lagerloef, G. S. L-
911 band passive and active microwave geophysical model functions of ocean surface winds and
912 applications to Aquarius retrieval. *IEEE Transactions on Geoscience and Remote Sensing*, 51, 4619–
913 4632. doi:10.1109/TGRS.2013.2266915, 2013

914 Yueh, S. H., Tang, W., Fore, A., Hayashi, A., Song, Y. T., and Lagerloef, G. Aquarius geophysical
915 model function and combined active passive algorithm for ocean surface salinity and wind retrieval.
916 *Journal of Geophysical Research: Oceans*, 119, 5360–5379. doi:10.1002/2014JC009939, 2014

917 Zhang, H., Menemenlis, D. and Fenty, G. ECCO LLC270 Ocean-Ice State Estimate.
918 doi:1721.1/119821,2018

919 Zweng, M.M, Reagan, J.R., Seidov, D., Boyer, T.P., Locarnini, R.A., Garcia, H.E., Mishonov, A.V.,
920 Baranova, O.K., Weathers, K.W., Paver, C.R. and Smolyar, I.V. *World Ocean Atlas 2018, Volume 2:*
921 *Salinity*. A. Mishonov, Technical Editor, NOAA Atlas NESDIS 82, 50pp., 2019

922 Aman, A. A., Cman, C., and Bman, B. B.: More test articles, *J. Adv. Res.*, 35, 13–28,
923 doi:10.2345/67890, 201